Towards uniformly distributed heat, mass and charge

A flow field design study for high pressure and high current density operation of PEM electrolysis cells

Olesen, Anders Christian; Frensch, Steffen Henrik; Kær, Søren Knudsen

Published in:
Electrochimica Acta

DOI (link to publication from Publisher):
10.1016/j.electacta.2018.10.008

Publication date:
2019

Document Version
Accepted author manuscript, peer reviewed version

Towards uniformly distributed heat, mass and charge: A flow field design study for high pressure and high current density operation of PEM electrolysis cells

Anders Christian Olesen[a,*], Steffen Henrik Frensch[a], Søren Knudsen Kær[a]

[a]*Department of Energy Technology, Aalborg University, Pontoppidanstræde 111, 9220 Aalborg East, Denmark*

Abstract

In this work, a state-of-the-art, full-scale, Proton Exchange Membrane (PEM) electrolysis cell model is presented. The developed three-dimensional (3D) model accounts for compressible, two-phase flow including species, heat and charge transport in the anode and membrane. By incorporating electrochemistry as well as detailed heat and two-phase flow transport phenomena, the model is capable of studying cells at full-scale and for high current densities with high accuracy. To enable the modeling of thin catalyst layers (CL) for high current density operation in a 3D framework, the CL is modeled as an interfacial boundary.

The necessary electrochemical parameters are obtained by fitting polarization curves of a two-dimensional version of the devised model to experimental measurements from a small cell. It is found that the obtained parameters are in agreement with literature values and that the fitted model is able to capture the performance for temperatures from 323 to 353 K and for current densities up to $5\,\mathrm{A\,cm^{-2}}$. Furthermore, it is identified that for high current density operation, three types of overpotential losses are nearly equally dominant: the anode kinetics, the PEM ohmic resistance and the non-membrane ohmic resistance due to poor electrical contact between layers and current constrictions in the CL.

The developed 3D model is applied to three different circular, interdigitated anode flow fields aimed a high pressure and high current density operation. When operating the cell at a cathode pressure of 100 bar, a current density of 5 A $\mathrm{cm^{-2}}$ and stoichiometric constant of 350, it is found that the cell potential shows little dependence on the applied flow field. However, large in-plane variations can occur that may impact lifetime significantly. Particularly for the temperature field, an in-plane difference of up to 20.2 K relative to the intended cell temperature is found in the worst case. For all three cases, the occurrence of hot spots is linked to the maldistribution of two-phase flow and current density. Out of the studied cases, it was found that equal land width between the channels gives the best distribution of charge, mass and heat.

Keywords: Electrolysis, PEM, gas-liquid flow, full-scale, modeling, high current density

1. Introduction

The research into proton exchange membrane electrolysis cells (PEMEC) has gained increasing attention in recent years [1]. This focus has partially been sparked by a global interest in hydrogen as a means of storing and carrying energy [2]. Although hydrogen production through electrolysis has reached a level that can be considered commercially available, the production capacity is still too low to meet the requirements set by the vision of a hydrogen economy. Meanwhile, the investment and operation cost of producing hydrogen also need to be lowered significantly to make it feasible [2]. One means of lowering the investment cost could be to increase the operating current density and thus lower the cost per produced unit mass of hydrogen. Already today commercial manufacturers of PEM electrolysis cells like Giner ELX or Proton Onsite Inc. have moved away from a nominal operating current density of $1\,\mathrm{A\,cm^{-2}}$ and towards 2-3 $\mathrm{A\,cm^{-2}}$ [3, 4]. Moreover, there is an interest in moving towards even higher current densities of up to $5\,\mathrm{A\,cm^{-2}}$. In fact, Lewinskia et al. [5] from 3M showed that it potentially can become feasible to operate beyond a current density of $10\,\mathrm{A\,cm^{-2}}$. A concern, then, would be whether heat and gas management is significantly impeded. In order to investigate this in more detail, there is a need for developing mechanistic, multi-phase flow models for predicting the species transport in porous media and channels, as pointed out by Carmo et al. [1] in their review on PEM electrolysis. Before addressing modeling, it is meaningful to review the literature on experimental, two-phase flow studies relevant for PEM electrolysis cells.

For PEM electrolysis cells, only few experimental studies have so far targeted the impact of two-phase flow phenomena in channels on the electrochemical performance. This is somewhat surprising, since, depending on flow con-

*Corresponding author

Email addresses: aco@et.aau.dk (Anders Christian Olesen), shf@et.aau.dk (Steffen Henrik Frensch), skk@et.aau.dk (Søren Knudsen Kær)

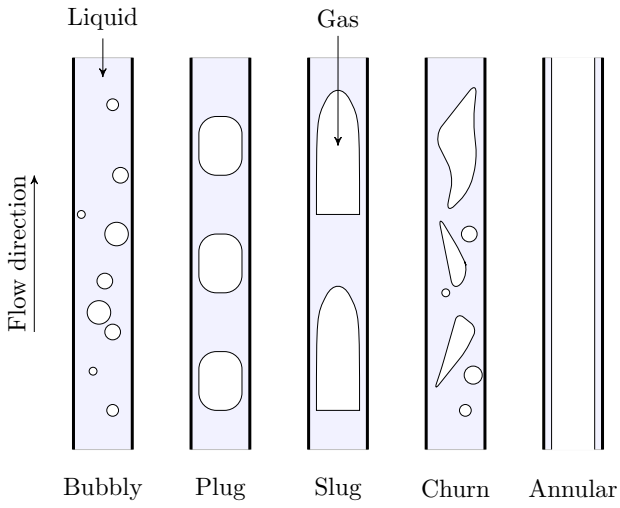

Figure 1: An overview of two-phase flow patterns typically found in the channels of a PEMEC flow field

ditions, very different two-phase flow pattern are likely to occur. Depending on the gas-flow pattern, heat and mass transfer will be affected differently. An overview of the most common gas-liquid flow patterns is schematically illustrated in figure 1.

To investigate the coupling between gas-liquid flow pattern in channels and cell performance, Ito et al. [6] studied the behavior of single-channel serpentine, dual-channel serpentine and parallel channels. A comparison of polarization curves (i.e. voltage vs. current), indicated that performance is improved by increasing the number of parallel channels. The improvement was attributed to lower superficial velocities, which subsequently changes the two-phase flow pattern from being annular or slug to bubbly. To identify this shift in two-phase flow pattern, Ito et al. [6] used the flow map by Mishima and Hibiki [7] for a diameter of D =2.05 mm, although their channels had a hydraulic diameter of 1 mm. In a study that followed, Ito et al. [8] furthermore investigated the effect of the porous transport layer (PTL) properties on the two-phase flow in channels. It was found that decreasing the pore size until a limit of 20 µm resulted in an improved electrochemical performance. This effect was attributed to a smaller detachment bubble diameter, which leads to shorter slugs and hereby a lowered bubble coverage of the PTL. As a part of their work, they furthermore did a more extensive literature survey on two-phase flow pattern in comparison to their previous work in ref. [6]. They concluded on the basis of flow maps by Ide et al. [9] and Cubaud and Ho [10] that it is only at very high liquid superficial velocities that dispersed bubbly flow can be expected. At low liquid superficial velocities it is more likely to expect plug flow. Moreover, they discussed experimental evidence that suggests that the transition boundary between plug and slug flow is moved depending on the detachment bubble diameter.

Later, Dedigama et al. [11] conducted an *in-situ* visualization study of the gas-liquid, two-phase flow using a transparent PEM electrolysis cell with a hydraulic diameter of 2.5 mm and compared their findings to the flow map by Mishima and Hibiki [7] for a diameter of 2.05 mm. Their measurements appeared to align well with the applied reference flow map. Bubbly flow was observed until a current density of $1\,\mathrm{A\,cm^{-2}}$. The lower the liquid superficial velocity, the larger bubbles appeared, suggesting a transition to plug flow. Interestingly, it is concluded in contrary to the work by Ito et al. [6] that switching from bubbly to slug flow improves cell performance due to improved mass transfer. This conclusion is drawn on the basis of their electrochemical impedance spectroscopy (EIS) measurements that show an increase in the second arc of their Nyquist plots with increasing liquid superficial velocity. Meanwhile, it should be noted that the change in the second arc is only attributed to mass transport in their work. Nothing is mentioned about the fact that the temperature changes and that this affects charge transfer, which may be a more straightforward explanation of the observed trend. Moreover, it should be noted that their Nyquist plot at high current densities shows a high extent of scatter, which makes it questionable what can be concluded through this data.

On the two-phase flow in porous media of PEM electrolysis cells, a few studies have also been conducted. Selamet et al. [12] studied the gas-liquid, two-phase flow within the PTL using neutron imaging and optical visualization. They observed two types of flow behavior. One where gas builds up and is released periodically, and another where gas is stagnant and transport of water is blocked. Their findings further showed that a higher gas volume fraction is visible towards the outlet and that gas removal is improved by increasing the water stoichiometry, i.e. the amount of inlet water relative to a given current density. In the work by Arbabi et al. [13], a two-dimensional, pore-network representation of a PTL was build and used for studying the air bubble transport using optical visualization. It was found that the flow remains capillary-dominated even at high gas flow rates. In conclusion, they underlined that further studies were necessary to determine which type of PTL structure is preferable. To investigate the behavior of an operating cell, Hoeh et al. [14] studied the gas-liquid, two-phase flow of a serpentine anode flow field using synchrotron X-ray radiography. Their findings revealed that transport of gas goes through specific pathways and the number of these increases with current density. Hence, they concluded that the saturation of water within the PTL depends on current density. The same observation was made by Lafmejani et al. [15]. In their experimental work, the two-phase flow behavior of PEM electrolysis cell was studied *ex-situ* by blowing oxygen through a fibrous titanium felt layer attached to a single channel with liquid water flowing. Synchrotron X-ray radiography was further used in-situ in another study by Hoeh et al. [16] to measure the local, time-averaged,

gas volume fraction within the micro-channels. It was found that the time-averaged, gas volume fraction gradually increases towards the outlet. Moreover, it was seen that the gas volume fraction increased with increasing current density, and decreased with increasing liquid mass flow rate. To study the gas-liquid, two-phase flow in the through-plane direction of the membrane electrode assembly (MEA), Seweryn et al. [17] used neutron radiography. They found for sintered titanium that the volume averaged, gas volume fraction profile through the PTL essentially remains constant across a large range of operating current densities in contrary to the findings of Hoeh et al. [14]. Hence, no sign of water-starvation was seen at any point. The impact of water stoichiometric ratio and thus the effect of two-phase flow was recently studied by Immerz et al. [18]. In their work, it was clearly seen that for a too low water stoichiometric ratio, a large inhomogeneous current density and temperature distribution was observed. Hence, their findings clearly underline the importance of correctly managing the water flow, if hot spots and large current density fluctuations are to be avoided.

In order to further investigate the impact of two-phase flow on the behavior of PEM electrolysis cells, simulation studies have likewise been carried out. These have so far mainly focused on the PTL or one-dimensional effects [19]. Only very few studies have in fact investigated the three-dimensional behavior within channels and porous media of PEM electrolysis cells. In the work by Nie and Chen [20], the authors investigated the two-phase flow distribution within a parallel channel anode flow field. Their model was based on a multi-phase mixture formulation that applies an algebraic slip condition between fluid phases and hence only models a single momentum equation. To simplify their model, the presence of the MEA as well as the bipolar plate (BPP) was excluded, and the flow of gas was assumed to be bubbly flow. Their findings revealed that re-circulation zones could occur when using a parallel channel configuration. Moreover, severe maldistribution phenomena were observed that could potentially lead to gas accumulation and hot spots. In the work by Olesen et al. [21] a two-fluid model that solves one set of conservation equation for each phase was developed for studying gas-liquid flow within channels and PTL. The model, moreover, accounted for heat transfer as well as turbulence. Similarly to Nie and Chen [20], the presence of the BPP was ignored and the flow of gas was assumed to be bubbly. Using a circular, interdigitated flow field the authors studied two-phase flow and heat maldistribution. Their results showed that the heat distribution under the simulated conditions was very sensitive to the particle diameter of the gas bubbles within the channels. Moreover, lowering the water stoichiometry greatly increased the impact of the gas production on the heat and flow maldistribution. To model the two-phase flow within the PTL in more detail, Arbabi et al. [22] applied a volume-of-fluid (VOF) model to investigate the same conditions they had previously studied experimentally in ref. [13]. Their simulation results showed good agreement with the experimental results, with only minor discrepancies when comparing saturation behavior. Bubble transport was found to be capillary-dominated, as expected. To study the coupling effect between gas-liquid flow in the channels and PTL of an interdigitated flow field, Lafmejani et al. [23] developed a three-dimensional, VOF model. Although their model neglected capillary pressure effects within the PTL, their simulation results still revealed that oscillating transition from slug, plug and bubble flow in the outgoing channels impacted the distribution of liquid water within the PTL.

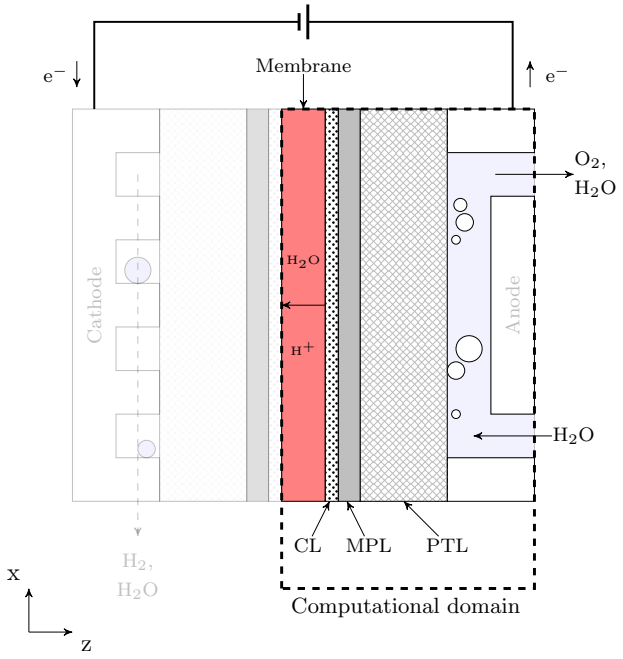

Figure 2: Cross-sectional schematic of a PEM electrolysis cell. The dashed line marks the computational domain of the conducted study.

Based on the conducted literature review, it can be concluded that there are many contradictory experimental observations of the impact and behavior of two-phase flow in PEM electrolysis cells. Of these discrepancies, many can potentially be refuted or confirmed through modeling. Before mathematical models can do so, further model development is however needed. Another aspect revealed by this literature survey is that modeling activities on full-scale PEM electrolysis cells are very scarce. This is surprising since there is an obvious need for simulating the effect of up-scaling to real size cells, rather than only studying representative one- or two-dimensional models that do not capture the inherent three-dimensional phenomena at play. This issue is particularly predominant at high current densities, where temperature and two-phase flow maldistribution phenomena become even more severe.

With the lack of full-scale modeling activities there has similarly not been published any studies that give detailed guidelines on how to design flow fields for PEM electrolysis

cells. Hence, there is a knowledge gap on how an even charge, mass and heat distribution can be achieved that ensures a high durability.

In order to address these before mentioned issues, an enhanced two-fluid model is developed. The improvements are in particular aimed at better capturing the heat transport and two-phase flow phenomena that are observed experimentally under the prescribed conditions. Alongside these improvements, the two-fluid model includes transport of ions and electrons as well as electrochemistry. The previously studied modeling domain in ref. [21] is also expanded to include current distributor (CD), BPP, microporous layer (MPL), CL and PEM, as is schematically drawn in figure 2.It should be noted that the CL is not resolved, since the thickness is less than 5 µm in the applied reference cell that is used for obtaining the electrochemical parameters. This means that a thin film model is applied. The developed model is then applied to investigate the discussed re-design strategies of ref. [21] in order to mitigate mass and heat maldistribution for circular, interdigitated flow fields that are suitable for asymmetric high pressure and current density operation. A goal of the present research effort is to evaluate the feasibility of applying a state-of-the-art PEMEC for high current density operation.

In the following, the cell designs and the possible two-phase flow patterns within the channels are examined. Then, the mathematical model including conservation and closure equations are presented. Hereafter, the needed electrochemical parameters are obtained by fitting a two-dimensional formulation of the devised model to polarization curves across multiple temperatures and a large range of current densities. Finally, a flow field design comparison is carried out using the devised three-dimensional model at a current density of $5\,\mathrm{A\,cm^{-2}}$, constant stoichiometry coefficient of 350 and a temperature of 70 °C. Furthermore, each cell is operated asymmetrically compressed in order to minimize the energy consumption related to the mechanically compression of hydrogen. The cathode is operated at 10 MPa and the anode at 0.3 MPa. This leads to a differential pressure of 9.7 MPa. The applied asymmetric compression makes the PEM and anode PTL subject to a large compression force that alters the thickness of the layers and changes transport properties as discussed in ref. [24, 21]. This effect is included in the modeling work.

2. Cell design and two-phase flow considerations

The three investigated interdigitated anode flow fields are visible in figure 3. The three flow fields are denoted Case A, Case B and Case C from left to right. Case A has straight channels with equal spacing, Case B has straight channels with land areas of equal size, and Case C has round channels with land areas of equal size. The associated dimensions of the cells can be found in Table 1.

Case A represents the classical approach from the design of interdigitated flow fields for fuel cell application, where the distance between channels is kept constant. Case B is an attempt to make the distribution of liquid water between channels more uniform. This is attempted by making the distribution of porous medium flow resistances between the in- and outgoing channels more uniform. In case C, rounded channels are applied to counteract the effect that an interdigitated flow field with straight channels tends to create a parabolic shaped velocity distribution underneath the land area along the length of the channels, with the highest velocities found near the beginning and the end of the channels.

Parameter	Value	Unit
Land to area	0.75	-
Channel depth	0.6	mm
Channel width	1	mm
Manifold depth	0.6	mm
Manifold width	2.5	mm
Cross-sectional area of cell	56.75	$\mathrm{cm^2}$
Cross-sectional area of CD and BPP	105.68	$\mathrm{cm^2}$
Thickness of PTL at 10 MPa compression	300[a]	µm
Thickness of MPL	40	µm
Thickness of BPP	1.6	mm
Thickness of CD	4	mm
Thickness of dry Nafion 117	178	µm

Table 1: Geometrical properties of the flow fields. [a]The thickness of the PTL was measured in ref. [21]

In all three cases, the land to void ratio is the same with approximately 0.75. This value has been selected to ensure the mechanical strength of the ribs when running a cell asymmetrically pressurized with a pressure difference of up 20 MPa.

Each interdigitated channel of the flow field has a depth of 0.6 mm and a width of 1 mm. This amounts to a hydraulic diameter of 0.75 mm. The manifold channels have the same depth, but with a larger width of 2.5 mm. This mans that the hydraulic diameter has a slightly higher value of 0.96 mm. The outgoing channels have been numbered from left to right as seen in figure 3. It should be noted that for the investigated operating conditions and channel dimensions, the Reynolds number out of the cell is 30500. For the end of the outgoing interdigitated channels, the Reynolds number is on average 7260.

The membrane electrode assembly (MEA) modeled in this work, is based on the design of the commercial manufacturer EWII Fuel Cell A/S. In their MEA design, the anode consists of a PTL, MPL and CL. The PTL is made from a fibrous titanium (Ti) felt, the MPL consists of a $2.7\,\mathrm{mg\,cm^{-2}}$ iridium (Ir) and the CL of a combination of $0.08\,\mathrm{mg\,cm^{-2}}$ Nafion binder and $0.3\,\mathrm{mg\,cm^{-2}}$ iridium oxide (IrO_2). The PEM in the MEA is Nafion 117.

It should be noted that the MPL was originally added to provide an improved electric contact. Moreover, it was assumed that the layer was electrochemically inactive, however it has later been shown not to be the case as discussed

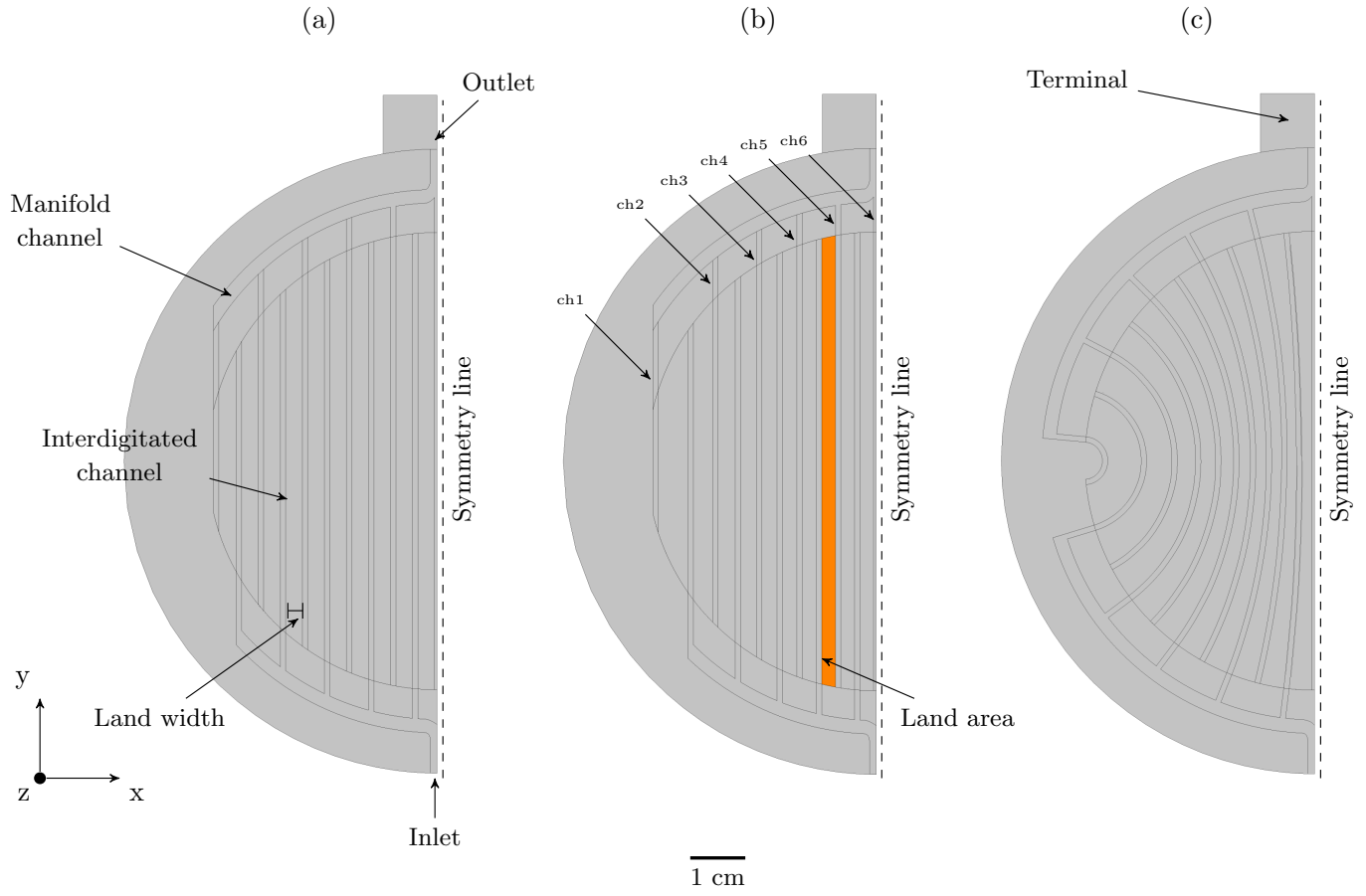

Figure 3: Three variation of a circular, interdigitated anode geometry: (a) equal land width, (b) equal land area, and (c) equal land area with half the area of case b.

by Elsøe et al. [25] in their erratum. From the work by Elsøe et al. [25], it can further be seen from backscattered electrons SEM images that the a clear interface between the MPL and CL is not visible.

In addition to the before mentioned components, EWII Fuel Cell apply two BPP and two CD when testing their cells. The anode BPP is manufactured from Ti and both CDs from gold coated copper (Cu). The same materials are applied to the BPP and CD in this study. For more information on the MEA design and its structural properties, the reader is referred to ref. [25]. For specific information on the PTL, the reader referred to ref. [21]. Here, the thickness, porosity and permeability as function of compression are determined. For information on the contact losses between the components as a function of compression, the reader is referred to ref. [26].

The active cross-sectional area of the cells investigated in this study is 56.75 cm^2. The thicknesses of the CD and BPP are 4 and 1.6 mm, respectively. The thickness of the MPL is 40 µm, although the backscattered electrons SEM images taken by [25] show a combined thickness of the MPL and CL between 4 - 7 µm. The thickness of the MPL is overestimated to make it easier to numerically model the capillary pressure across the PTL and MPL interface. Furthermore, because of the small CL thickness, i.e. less than 4 µm, it is not meaningful to spatially resolve the ionic electrical potential field in the through-plane direction in a three-dimensional CFD framework. Hence, in this work, the CL is treated as an thin film, which means that the layer is modeled as an interfacial boundary condition.

A limitation of the previous developed model was that the presence of the CD, BPP and the PEM was not include in the modeling domain. By adding these components, a more accurate prediction of the thermal distribution can be obtained.

2.1. Gas-liquid flow in channels

When doing a literature survey of the most recent studies on gas-liquid flow in PEM electrolysis cells, it becomes apparent that channels are often classified as being either mini- or micro-channels, since the investigated hydraulic diameters typically range from 2.5 mm down to 0.8 mm [6, 11, 21, 20, 23]. In fact, the two classifications are often used synonymously in the available literature about the same hydraulic diameters, since a clear distinction seems not to exist. Meanwhile, such a distinction is important since mini-channels essentially behave like ordinary channels, while micro-channels do not [27]. The difference be-

tween mini- and micro-channels is primarily due to surface tension forces becoming dominant over inertia forces. This change makes bubbles less susceptible to coalescence and break-up and hence alters the location of the transition lines between the different flow patterns and suppresses stratified flow[28]. As discussed by Shao et al. [28] in their extensive review of micro-channels, many attempts have been made in order to define criteria for the transition to microchannel flow. A few of those are based solely on the diameter [29, 30], some on the Eötvös number [31] and others on a series of dimensionless numbers [32]. When comparing the different criteria, the transition from mini- to micro-channel flow is predicted in a range from 3 mm down to 200 µm for air-water systems. Thus, it appears that channels found in PEM electrolysis cells overlap with this transition region. Hence, care should be applied when comparing two-phase flows across various hydraulic diameters in this range, since the two-phase flow behavior may significantly change.

Based on the designed geometry and two different operating conditions, i.e. constant stoichiometry and constant flow, the corresponding superficial velocities are plotted in figure 4. This is done alongside the flow pattern maps for vertical flow in triangular shaped channels with a hydraulic diameter of 1.433 and 0.833 mm measured by Zhao and Bi [33]. It should be noted that the flow pattern maps by Zhao and Bi [33] have been chosen, since these show the highest degree of similarity with the channels studied in this work.

Under the constant stoichiometry condition, a value of 350 is specified. For constant flow, a liquid flow rate relative to a current density of 1 A cm^{-2} and a stoichiometry coefficient of 350 is specified. In the calculation of the mass flows, the evaporation of water is included, as opposed to the previous flow map studies for PEM electrolysis that disregarded this effect [6, 8, 11]. It should be noted that at 70 °C and 1 atm, the gas volume flow rate is in fact increased by 28 % assuming a fully saturated gas flow. The increase in volume flow due to evaporation can simply be calculated by specifying the saturation pressure of water according to the operating temperature while applying Daltons law of partial pressures and the definition of water activity for an ideal gas. Doing so yields the mole fraction of water in the gas phase:

$$x_{\mathrm{H_2O},g} = \frac{p_{sat,\mathrm{H_2O}}}{P_{anode}} \tag{1}$$

The mass flow rates out of the cell as a function of stoichiometric coefficient and current are then calculated by setting up a mass or mole balance and applying Faradays first law as well as equation 1:

$$\begin{aligned} \dot{m}_{l,out} &= \dot{m}_{\mathrm{H_2O},gen} - \dot{m}_{\mathrm{H_2O},evap} && (2)\\ &= \frac{I M_{\mathrm{H_2O}}}{2F}\left(\lambda - 1 - \frac{x_{\mathrm{H_2O},g}}{1 - x_{\mathrm{H_2O},g}}\right) && (3) \end{aligned}$$

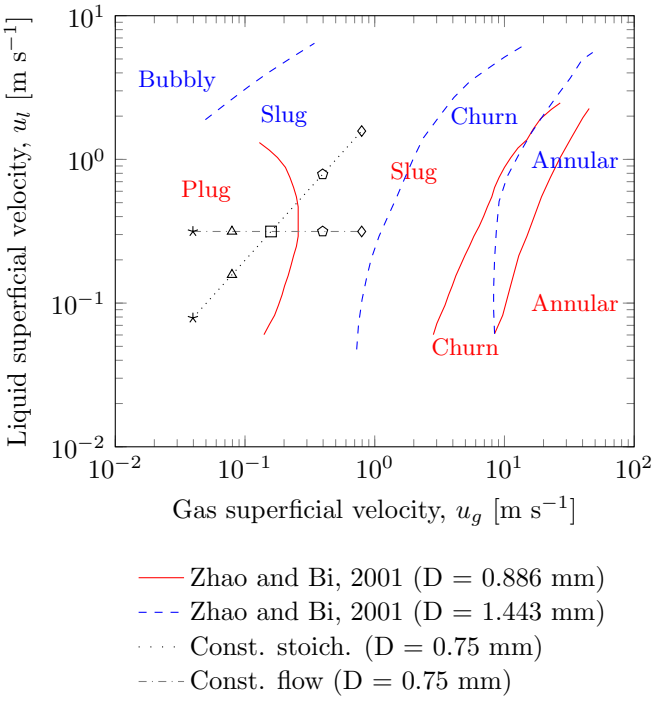

Figure 4: Flow pattern maps based on data from Zhao and Bi [33]. The solid and dashed lines denote transition lines between the various flow pattern. The symbols denote the resulting flows for different current density operations: (⋆) 0.25 A cm^{-2}, (△) 0.5 A cm^{-2}, (□) 1 A cm^{-2}, (⬠) 2.5 A cm^{-2} and (◇) 5 A cm^{-2}.

$$\begin{aligned} \dot{m}_{g,out} &= \dot{m}_{\mathrm{O_2},gen} + \dot{m}_{\mathrm{H_2O},evap} && (4)\\ &= \frac{I}{4F}\left(M_{\mathrm{O_2}} + M_{\mathrm{H_2O}}\frac{x_{\mathrm{H_2O},g}}{1 - x_{\mathrm{H_2O},g}}\right) && (5) \end{aligned}$$

Here I is the current (A), F is Faraday's constant (C mol^{-1}), λ is the stoichiometry coefficient of water, M is the molecular weight (kg $kmol^{-1}$), $\dot{m}_{\mathrm{H_2O},co}$ denotes the mass flow due to water crossover (kg s^{-1}), $\dot{m}_{\mathrm{H_2O},evap}$ is the amount of water evaporated (kg s^{-1}). Based upon these outlet mass flow rates, the superficial velocities out of each are calculated as follows assuming that all the flow of water and gas is distributed equally among all channels:

$$u_g = \frac{\dot{m}_{g,out}}{N_{ch} A_{cs} \rho_g} \tag{6}$$

$$u_l = \frac{\dot{m}_{l,out}}{N_{ch} A_{cs} \rho_l} \tag{7}$$

Here u is the superficial velocity (m s^{-1}), N_{ch} is the number of channels, A_{cs} is the cross-sectional area (m^2) and ρ is density (kg m^{-3}).

By examining the two operating conditions and the specified current densities, it appears that the two conditions lead to the same trend. For a diameter of 1.443 mm, it is seen that the flow remains slug flow in the whole operating regime. This is in contrary to a diameter of

0.866 mm, where a transition in two-phase flow pattern from plug to slug flow occurs when the current density is increased. The same trend occurs for both constant stoichiometry and constant flow.

One circumstance that makes the discussion of flow maps difficult is that a decreasing hydraulic diameter essentially changes the location of the transition lines between flow patterns. Hence, in terms of two-phase flow, completely different flow patterns are found for a specific set of superficial velocities. Another issue is that both superficial velocities change along the channel length for an interdigitated flow field. This implies that plug flow could occur particularly towards the beginning of the channels for a diameter $D \leq$0.866 mm. For larger channels, it would also imply that slug flow would occur no matter the circumstance.

Another issue that affects the observed flow pattern is the fact that gas is released relatively evenly across the active surface area, which means that the beginning of a channel would see less gas then the outlet of a channel.

For the specific channel dimensions investigated in this study, Lafmejani et al. [23] found experimentally and by VOF simulations that there is large span in gas bubble size. Moreover, it appears that bubbles coalesce into plugs and eventually become long slugs over time and along the length of a channel,. This means that bubbles tend to change size from down to 0.1 mm up to 0.8 mm before turning into cylindrical bubbles that are 8 to 10 mm long. For a cylindrical bubble, these dimensions lead to a Sauter mean diameter of around 1.15 mm.

From a modeling point of view, this means that it is an oversimplification to assume only spherical bubbles with a Sauter mean diameter of 0.1 mm or less, as was done in our previous work in ref. [21] and in the work by Nie and Chen [20]. Moreover, it underlines that the application of a dispersed-continuous, two-fluid formulation is perhaps too crude. Nonetheless, it is still a necessary simplification to take in order to develop a model that can be used for parametric studies of stacks and or even single cells. At this time, a VOF model that resolves the interfacial surface area is simply assessed too computational expensive for large-scale simulations of PEM electrolysis cells. To address the existence of both bubbles and slugs within the flow, hydrodynamic forces are made dependent on a simplified flow pattern transition model.

3. Mathematical model

The mathematical model presented in this work is a continuation of the two-fluid model development in ref. [21]. While the previous model accounted for turbulence and thermal heat transport, phenomena such as phase change, charge transport and reaction kinetics where ignored at that stage of the development process. Thus, all the added physical phenomena are explained in the following subsection.

3.1. Conservation equations

The conservation equation presented in this work have been derived in accordance with the two-fluid approach, where the instantaneous, microscopic transport equations have been time or volume averaged in order to derive a macroscopic Euler-Euler formulation. For details, the reader is referred to Ishii and Hibiki [34] and Jakobsen [35].

3.1.1. Continuity

In continuum fluid mechanics, mass conservation is modeled using continuity equations. In the two-fluid model, one continuity equation is solved for each phase as follows:

$$\nabla \cdot (\varepsilon s_g \rho_g \mathbf{U}_g) = \Gamma_{O_2,g} - \Gamma_{gl} \tag{8}$$

$$\nabla \cdot (\varepsilon s_l \rho_l \mathbf{U}_l) = \Gamma_{H_2O,l} + \Gamma_{gl} \tag{9}$$

Here s is the phase volume fraction, ε is the volume porosity, $\mathbf{U}$ is the true phase velocity ($\mathrm{m\,s^{-1}}$), ρ is the phase density ($\mathrm{kg\,m^{-3}}$), Γ_A is the volume specific mass flow rate due to an electrochemical reaction involving species A ($\mathrm{kg\,s^{-1}\,m^{-3}}$) and Γ_{gl} is the specific mass flow rate due to phase change of water ($\mathrm{kg\,s^{-1}\,m^{-3}}$).

3.1.2. Momentum

The momentum conservation for the gas and liquid phases are modeled in the following fashion:

$$\begin{aligned} \nabla \cdot (\varepsilon s_g \rho_g \mathbf{U}_g \mathbf{U}_g) \quad = \quad & \nabla \cdot (\varepsilon s_g \tau_g) - \varepsilon s_g \nabla p_l \\ & ... + \delta_{pm} \varepsilon s_g \nabla p_c + \varepsilon s_g \rho_g \mathbf{g} - \mathbf{M}_{lg} \\ & ... + \delta_{pm} \frac{s_g^2 \varepsilon^2 \mu_g}{K k_{rel,g}} \mathbf{U}_g \end{aligned} \tag{10}$$

$$\begin{aligned} \nabla \cdot (\varepsilon s_l \rho_l \mathbf{U}_l \mathbf{U}_l) \quad = \quad & \nabla \cdot (\varepsilon s_l \tau_l) - \varepsilon s_l \nabla p_l \\ & ... + \varepsilon s_l \rho_l \mathbf{g} + \mathbf{M}_{lg} \\ & ... + \delta_{pm} \frac{s_l^2 \varepsilon^2 \mu_l}{K k_{rel,l}} \mathbf{U}_l \end{aligned} \tag{11}$$

Here τ_g is the viscous shear stress term (Pa); p_l and p_c are the liquid and capillary pressure (Pa), $\mathbf{g}$ is the gravimetric vector ($\mathrm{m\,s^{-2}}$), $\mathbf{M_{lg}}$ is the interfacial momentum transfer from liquid to gas phase ($\mathrm{kg\,m^{-2}\,s^{-2}}$), δ_{pm} is a function that is 1 within the porous media and zero elsewhere, μ is dynamic viscosity (Pa s), K is the viscous permeability $\mathrm{m^2}$) and k_{rel} is the relative permeability. The capillary pressure and relative permeability is modeled using van Genuchten relations similarly as in ref. [21].

3.1.3. Species

If the extent of hydrogen crossover through the electrolyte membrane is low compared to the production of oxygen, the gas phase of the anode can be assumed to primarily consist of two species: oxygen and water vapor. Since the number of species is $N = 2$ in the gas mixture,

there is only one independent mass fraction according to the mass fraction constraint:

$$\sum_{i=A}^{N} Y_i = 1 \tag{12}$$

This implies that only one species conservation equation needs to be solved. In this work, the following species conservation formulation is used for transport of water vapor:

$$\begin{aligned} \nabla \cdot (\varepsilon s_g \rho_g \mathbf{U}_g Y_{H_2O,g}) &= \nabla \cdot (\varepsilon s_g \mathbf{J}_{H_2O,g}) \\ &\quad ... + \varepsilon s_g S_g + \dot{m}_{gl} \end{aligned} \tag{13}$$

Here $Y_{H_2O,g}$ denotes mass fraction of water in the gas phase, and $\mathbf{J}_{H_2O,g}$ is the diffusive mass flux of water relative to a mass-averaged velocity ($\mathrm{kg\,s^{-1}\,m^{-2}}$). The diffusive flux is expressed in terms of Fick's first law of diffusion and includes an additional contribution due to turbulent diffusion [36]:

$$\mathbf{J}_{H_2O,g} = -\Gamma_{H_2O} \nabla Y_{H_2O,g} \tag{14}$$

$$\Gamma_{H_2O} = \rho_g D^{eff}_{H_2O,g} + \frac{\mu_{T,g}}{Sc_{T,g}} \tag{15}$$

Here Γ_{H_2O} is the molecular diffusion coefficient of water vapor ($\mathrm{kg\,s^{-1}\,m^{-1}}$), $D^{eff}_{H_2O,g}$ is the effective mass diffusion coefficient of water vapor ($\mathrm{m^2\,s^{-1}}$), μ_T is the turbulent viscosity (Pa s) and $Sc_{T,g}$ is the turbulent Schmidt number.

3.1.4. Charge

The flux of electrons and ions can in a simple manner be modeled through a Ohm's law formulation:

$$\mathbf{i}_s = -\sigma_{eff} \nabla \phi_s \tag{16}$$

$$\mathbf{i}_e = \kappa_{eff} \nabla \phi_e \tag{17}$$

Here the subscripts s and e denote solid and electrolyte phase, respectively, σ_{eff} and κ_{eff} are conductivities of the solid and electrolyte phases ($\mathrm{S\,m^{-1}}$), respectively, and ϕ is the electrostatic potential (V). For ions, this treatment may be a bit simplified, since it ignores an electrophoretic effect that can be significant for a highly swelled PEM according to concentrated solution theory [37]. Nevertheless, it gives a good starting point for the model development. The ion conductivity is dependent on the water content in the membrane as shown in table 2. However, for the sake of simplicity, it is assumed that the membrane water content is uniform and equal to the equilibrium water content of the liquid phase. As will be seen in the simulation results, a high volume fraction of liquid water close to the catalyst is ensured even at high current density, hence it is valid to assume a uniform membrane hydration. It should further be noted that since the cell is operated asymmetrically pressurized, the PEM is compressed according the to the pressure difference between the anode and cathode. Thus, the water content of the PEM is significantly decreases as shown by Kusoglu et al. [38]. For a liquid equilibrated PEM compression by 9.7 MPa, this leads to a water content $\lambda = 16.6$.

The conservation of electrons and ions can now be modeled as follows:

$$\nabla \cdot (\varepsilon_s \mathbf{i}_s) = R_{\mathrm{e^-}} \tag{18}$$

$$\nabla \cdot (\varepsilon_e \mathbf{i}_e) = R_{\mathrm{H^+}} \tag{19}$$

Here R is the reaction rate ($\mathrm{A\,m^{-3}}$).

3.1.5. Thermal energy

The transport of energy can be modeled in a simplified manner by neglecting volumetric and mechanical work. This is particularly meaningful for low velocities, since it improves convergence behavior. When doing so, the following thermal energy conservation equation can be obtained:

$$\begin{aligned} \nabla \cdot (\varepsilon s_g \rho_g \mathbf{U}_g e_g) &= \nabla \cdot \left(\varepsilon s_g \left(k_g + C_p \frac{\mu_T}{Pr_T} \right) \nabla T_g \right) \\ &\quad ... + \nabla \cdot \left(\varepsilon s_g \sum_{A=1}^{N_c} \Gamma_A e_A \nabla Y_{Ag} \right) \\ &\quad ... + h_{gl} \Gamma_{gl} + Q_{gl} + Q_{gs} \end{aligned} \tag{20}$$

$$\begin{aligned} \nabla \cdot (\varepsilon s_l \rho_l \mathbf{U}_l e_l) &= \nabla \cdot \left(\varepsilon s_l \left(k_l + C_{p,l} \frac{\mu_{T,l}}{Pr_{T,l}} \right) \nabla T_l \right) \\ &\quad ... - h_{gl} \Gamma_{gl} + Q_{lg} + Q_{gs} \end{aligned} \tag{21}$$

$$\begin{aligned} \nabla \cdot ((1-\varepsilon)\, \rho_s \mathbf{U}_s e_s) &= \nabla \cdot (\varepsilon s_s k_s \nabla T_s) \\ &\quad ... + \varepsilon_s \frac{|\mathbf{i}_s|^2}{\sigma_{eff}} + \varepsilon_e \frac{|\mathbf{i}_e|^2}{\kappa_{eff}} \\ &\quad ... + Q_{ec} + Q_{sg} + Q_{sl} \end{aligned} \tag{22}$$

Here e denotes static enthalpy (J), k is thermal conductivity ($\mathrm{W\,m^{-1}\,K^{-1}}$), and Q_{ec} is the heat dissipation due to electrochemical reactions ($\mathrm{W\,m^{-3}}$). It should be noted that the effect of Joule heating due ion and electron transport is included in equation 22.

3.1.6. Turbulence

To account for turbulence, Menter's Shear Stress Transport (SST) model is applied to the continuous liquid phase[39]. This type of turbulence model is a two-equation, eddy-viscosity turbulence model. It consist of two transport equations; one for turbulent kinetic energy k ($\mathrm{m^2\,s^{-2}}$) and one for turbulent eddy dissipation frequency ω ($\mathrm{s^{-1}}$):

$$\begin{aligned} \nabla \cdot (\varepsilon s_l \rho_l \mathbf{U}_l k) &= \nabla \cdot \left(\varepsilon s_l \left(\mu_l + \frac{\mu_T}{\sigma_k} \right) \nabla k \right) \\ &\quad ... + P_k - \beta' \rho k \omega + P_{kb} \end{aligned} \tag{23}$$

$$\begin{aligned} \nabla \cdot (\varepsilon s_l \rho_l \mathbf{U}_l \omega) &= \nabla \cdot \left(\varepsilon s_l \left(\mu_l + \frac{\mu_T}{\sigma_\omega} \right) \nabla \omega \right) \\ &\quad ... + \alpha \frac{\omega}{k} P_k - \beta \rho k \omega^2 + P_{\omega b} \end{aligned} \tag{24}$$

Here P_{kb} and $P_{\omega b}$ are the buoyancy turbulence production and dissipation terms ($m^2\ s^{-2}$), respectively, P_k is the turbulence production due to viscous forces, and $\beta = 0.075$, $\beta^{'} = 0.09$, $\alpha = 5/9$, $\sigma_k = 2$, $\sigma_\omega = 2$ are empirical constants. By solving these two transport equations, the turbulent viscosity of the liquid phase is then calculated as follows:

$$\mu_{T,l} = \rho_l \frac{k}{\omega} \tag{25}$$

For the gas phase, the dispersed phase zero equation model is applied as follows:

$$\mu_{T,g} = \frac{\rho_g}{\rho_l} \frac{\mu_{T,l}}{Pr_T} \tag{26}$$

Here Pr_T is the turbulent Prandtl number that relates the gas phase kinematic eddy viscosity to the liquid phase kinematic eddy viscosity.

3.2. Closure equations

In order to solve the depicted conservation equations, a set of algebraic equations are needed to create a consistent system of equations.

3.2.1. Mass transfer due to phase change

The phase change rate at the gas-liquid interface inside a porous medium can be treated as a mass convection problem, where only transport within the vapor phase is considered [40]. By further assuming that the vapor in the vicinity of the interface is in equilibrium with the liquid phase, the following formulation is obtained:

$$\Gamma_{gl} = -\Gamma_{lg} = a_{lg} h_{mass} \left(\rho_v - \rho_{sat}\right) \tag{27}$$

Here the subscripts v and sat stand for vapor and saturation, a_{lg} denotes the specific interfacial surface area between the liquid and gas phase (m^{-1}), ρ is density (kg m^{-3}), and h_{mass} is the mass convection coefficient (m s^{-1}), which can be expressed as a function of the dimensionless Sherwood number, Sh:

$$h_{mass} = \frac{Sh D_{H_2O,g}}{d} \tag{28}$$

Here $D_{H_2O,g}$ is the mass diffusion coefficient of vapor in the gas mixture ($m^2\ s^{-1}$) and d is the characteristic diameter of the pore (m). The Sherwood number for porous media found PEM fuel cells, which share a similar structure with the ones found in PEM electrolysis cells, has been estimated to be in the range of 2.04×10^{-3} to 2.45×10^{-1}[40].

The specific interfacial surface area can be correlated to the specific surface area of the pores and the phase volume fractions as follows:

$$a_{lg} = a_{pm} \varepsilon s_l s_g \tag{29}$$

Here a_{pm} refers to interfacial area between the solid phase of the porous medium and the void space (m^{-1}). The saturation density is calculated by assuming ideal gas behavior:

$$\rho_{sat} = \frac{P_{sat}}{RT} \tag{30}$$

Here P_{sat} is the saturation pressure (Pa) and R is the universal gas constant (J K^{-1} mol^{-1}). For a porous medium, where the capillary pressure can be substantial, the Kelvin equation can be used for correcting saturation pressure:

$$P_{sat} = P_{sat,0} \exp\left(\frac{p_c \overline{V}_{H_2O}}{RT}\right) \tag{31}$$

Here $P_{sat,0}$ is the saturation pressure of a planar surface (Pa) and $\overline{V}_w$ is the molar volume of water (m^3 mol^{-1}).

3.2.2. Mass and heat transfer due to electrochemistry

Although the oxygen evolution reaction (OER) consists of a complex series of reactions, the reaction current density can approximately be predicted by the following single Butler-Volmer equation, when surface coverage of intermediates and concentration effects can be neglected:

$$R = j_0 \left(exp\left(\frac{\alpha_a F}{RT}\eta\right) - exp\left(\frac{-\alpha_c F}{RT}\eta\right)\right) \tag{32}$$

Here R denotes the number of electrons transferred per volume (A m^{-3}), j_0 the exchange current density (A m^{-3}), α_a and α_c are the apparent charge transfer coefficients in the anode and cathode direction, respectively, F the Faraday's constant (J K^{-1} mol^{-1}) and η the activation overpotential (V). The overpotential is calculated as follows:

$$\eta = \phi_s - \phi_e - E_{eq} \tag{33}$$

Here E_{an} is the equilibrium potential (V).

The apparent charge transfer coefficients, which are dependent on the actual reaction mechanism, can be estimated if the rate determining step (RDS) has been identified and the remaining equations are assumed in quasi-equilibrium (QE), as follows [41]:

$$\alpha_a = \frac{n_b}{v} + n_{rds}\beta \tag{34}$$

$$\alpha_c = \frac{n_a}{v} + n_{rds}\left(1 - \beta\right) \tag{35}$$

Here n_b is the total number electrons before the RDS, n_a is the total number electrons after the RDS, n is the overall number of electrons transferred, v is the stoichiometric coefficient, i..e. the number of times the RDS has to occur for the overall reaction to take place once, and β is the charge transfer coefficient of the RDS.

For the OER on IrO_2, several mechanisms have been proposed in the literature. Of these, in particularly two seem worth mentioning: the three-step mechanism known as the electrochemical oxide path originally proposed by Bockris [42] and the four-step mechanism proposed by

Rossmeisl et al. [43]. While the electrochemical oxide path has been suggested on the basis of Tafel plots measured by Rasten et al. [44] and Slavcheva et al. [45], recent spectroscopic detection of the intermediate hydroperoxyl suggest the four-step mechanism [46]. For high current density operation, Slavcheva et al. [45] identified that the second deprotonation step in the electrochemical oxide path becomes the RDS:

$$\mathrm{H_2O} \rightleftharpoons \mathrm{OH}_{ads} + \mathrm{H}^+ + \mathrm{e}^- \tag{36}$$

$$\mathrm{OH}_{ads} \rightleftharpoons \mathrm{O}_{ads} + H^+ + \mathrm{e}^- \tag{37}$$

$$2\mathrm{O}_{ads} \rightleftharpoons \mathrm{O_2} \tag{38}$$

Inserting the values into equation 34 and 35 for the electrochemical oxide path, when the second step is the RDS, yields:

$$\alpha_a = 1 + \beta \tag{39}$$

$$\alpha_c = 1 - \beta \tag{40}$$

To take into account that the exchange current density is temperature and liquid phase volume fraction dependent, the following equation is implemented:

$$j_0 = s_l j_{0,T} \exp\left(\frac{-E_{act}}{R}\left(\frac{1}{T} - \frac{1}{T_{ref}}\right)\right) \tag{41}$$

The volumetric mass sink and source terms are formulated as a function of reaction current density as follows:

$$\dot{m}_{H_2O,l} = -\frac{MW_{H_2O}R}{2F} \tag{42}$$

$$\dot{m}_{O_2,g} = \frac{MW_{O_2}R}{4F} \tag{43}$$

The reversible and irreversible heat production associated with the electrochemical reaction is given by:

$$Q_{ec} = R\left(\eta - \frac{\Delta s}{4F}\right) \tag{44}$$

Here Δs is the change in entropy for the OER (J K^{-1}).

3.2.3. Interfacial momentum transfer

For two-phase flow in micro-channels, the interfacial momentum transfer term is dominated by drag, virtual mass and turbulent dispersion:

$$\mathbf{M}_{lg} = -\mathbf{M}_{gl} = N_d\left(\mathbf{f}_D + \mathbf{f}_V + \mathbf{f}_T\right) \tag{45}$$

Here N_d accounts for the number of particles per unit volume and $\mathbf{f}_D$, $\mathbf{f}_V$ and $\mathbf{f}_B$ are the drag force, virtual mass force and turbulent dispersion force, respectively.

The skin and form drag between two fluid phases can be described as a function of slip velocity and the drag coefficient:

$$\mathbf{f}_D = a_{lg}\rho_l C_d \left|\mathbf{U}_l - \mathbf{U}_g\right|\left(\mathbf{U}_l - \mathbf{U}_g\right) \tag{46}$$

Here $\mathbf{U}_{slip} = |\mathbf{U}_l - \mathbf{U}_g|$ denotes the slip velocity (SI unit: m/s), $a_{lg} = \phi_g\phi_l/d$ the specific surface area (m^{-1}), d the particle diameter (m), ρ_l the liquid density (kg m^{-3}) and C_d the drag coefficient. Throughout the domain, the two-phase flow pattern may change. This possible evolution from one pattern to another means that the drag coefficient changes.

For gas bubbles in a microchannel, it can be assumed that their shape is spherical (i.e. in the viscous regime) and non-distorted, since bubbles with a diameter less than the Raleigh-Taylor wavelength behave like solid spheres [47]. This means that the drag coefficient is dependent only the Reynolds number [34]:

$$C_{d,sphere} = \frac{24}{Re}\left(1 + \frac{1}{6}Re^{\frac{2}{3}}\right) \tag{47}$$

$$Re = \frac{d\rho_l\left|\mathbf{U}_l - \mathbf{U}_g\right|}{\mu_m} \tag{48}$$

$$\mu_m = \mu_l\left(1 - s_g\right)^{-1} \tag{49}$$

Here μ_m the mixture viscosity (Pa s), Re is the slip Reynolds number and d is characteristic bubble diameter (m).

For slug flow, the drag coefficient changes dependence. Instead of being dependent on slip Reynolds number, it correlates to the gas volume fraction and can simply be expressed as a power law function [34]:

$$C_{d,slug} = 9.1\left(1 - s_g\right)^3 \tag{50}$$

The virtual mass (i.e. the force needed to accelerate or decelerate a volume of the fluid phase surrounding an object as it moves through it) is modeled by the following relation:

$$\mathbf{f}_V = -s_g C_{vm}\rho_l\left(\frac{D\mathbf{U}_{slip}}{Dt} - \mathbf{U}_{slip}\cdot\nabla\mathbf{U}_l\right) \tag{51}$$

Here C_{vm} is the virtual mass coefficient, which for spheres and slugs, respectively, are given by [34]:

$$C_{vm,sph} = \frac{1}{2}\frac{1 + s_g}{1 - s_g} \tag{52}$$

$$C_{vm,slug} = 5\left(0.66 + 0.34\left[\frac{1 - D_b/L_b}{1 - D_b/3L_b}\right]\right) \tag{53}$$

Here D_b is the diameter of the slug and L_b is the length of the slug.

The turbulent dispersion (i.e. the force due to a concentration gradient) is modeled as the Favre-averaged interfacial drag force [48]:

$$\mathbf{f}_T = C_{TD}C_{lg}\frac{\mu_l}{\rho_l Pr_t}\left(\frac{\nabla s_g}{s_g} - \frac{\nabla s_l}{s_l}\right) \tag{54}$$

Here $C_{cd} = 1$ is a scaling coefficient.

Description	Symbol	Value / relation	Unit	Ref.
Cathode pressure	p_{cat}	10	MPa	-
Nominal outlet pressure for anode	$p_{an,out}$	0.3	MPa	-
Nominal outlet temperature	$T_{an,out}$	343.15	K	-
Average Sauter mean diameter in channels	D_{32}	1	mm	Exp.
Equilibrium potential	E_{eq}	$-\frac{\Delta G}{nF} - \frac{RT}{nF}\ln\left(p_{H_2}\sqrt{p_{O_2}}\right) - \frac{\Delta S}{nF}\left(T - T_0\right)$	V	Calc.
Ion conductivity of Nafion	κ_{eff}	$0.5\left(\phi_{H_2O} - 0.06\right)^{3/2}\exp\left(\frac{15000}{R}\left(\frac{1}{303} - \frac{1}{T}\right)\right)$	S cm^{-1}	[49]
Volume fraction of water in Nafion	ϕ_{H_2O}	$\lambda\bar{V}_{H_2O}/\left(\lambda\bar{V}_{H_2O} + \bar{V}_P\right)$	-	[38]
Volume fraction of polymer	ϕ_P	$\bar{V}_P/\left(\lambda\bar{V}_{H_2O} + \bar{V}_P\right)$	-	[38]
Swelled membrane thickness	L_{PEM}	$L_{dry}\left(\phi_P^{-1/3} - 1\right)$	m	[38]
PEM water content at a compression of 9.7 MPa	λ	15	-	[24, 38]
Molar volume of Nafion	$\bar{V}_P$	EW/ρ_{Nafion}	m^3 mol^{-1}	[38]
Electron conductivity of titanium	σ_{eff}	$1.3e^6$	S m^{-1}	
Fickian binary diffusion coefficient	$D^F_{H_2O,O_2}$	$2.5e^{-6}\left(\frac{P_{ref}}{P}\right)\left(\frac{T}{T_{ref}}\right)^{3/2}$	m^2 s^{-1}	[50]
Knudsen diffusion coefficient	$D^{Kn}_{H_2O}$	$\frac{d_{pm}}{3}\left(\frac{8RT}{\pi M_{H_2O}}\right)^{1/2}$	m^2 s^{-1}	[51]
Effective diffusion coefficient	$D^{eff}_{H_2O,O_2}$	$\frac{1}{\tau_p}\left(\frac{1}{D_{H_2O,O_2}} + \frac{1}{D_{Kn,H_2O}}\right)^{-1}$	m^2 s^{-1}	[51]
Tortuosity of PTL	τ_p	$s_g^{-1}\left(\frac{1-\varepsilon_p}{\varepsilon-\varepsilon_p}\right)^{0.785}$		[52]
Tortuosity of MPL	τ_p	$s_g^{-2}\varepsilon^{-1/2}$		[52]
Gravimetric vector	$\mathbf{g}$	$\begin{bmatrix} 9.81 & 0 & 0 \end{bmatrix}$	m s^{-2}	
Specific pore surface area	a_{pm}	1.0×10^6	m^{-1}	Assumed
Porosity of PTL	ε_{PTL}	0.77	-	[21]
Porosity of MPL	ε_{MPL}	0.71	-	Calc.
Permeability of MPL	K_{PTL}	2.25×10^{-11}	m^2	[21]
Permeability of MPL	K_{MPL}	1.0×10^{-13}	m^2	[53]
Break through pressure of the MPL	$P_{cb,MPL}$	80000	Pa	Assumed

Table 2: Modeling parameters and relations

3.2.4. Flow regime transition

For both drag and virtual mass, a transition scheme model is needed for identifying the two-phase flow pattern and hence when to apply which relation. One approach to identify the flow pattern is to track the interfacial area [34], however this is assessed too computational expensive taken the already complex model into consideration. A simplified approach, which by no means captures the dynamics of the transition process, could alternatively be to be applied an empirical switching correlation that depends on the volume fraction as well as channel diameter and orientation [47]. Although, these relationships are simple to implement and computational inexpensive, they are still relative crude estimates [34]. Furthermore, switching of the drag coefficient and interfacial area based on the gas volume fraction requires a blending function to avoid wiggles in solution field. Such an approach is among others seen in Höhne et al. [54] in their Algebraic Interfacial Area Density (AIAD) model. Finally, the last option is to use an empirical formulation similar to the universal drag law [47]. Such a formulation ensures a continuous transition behavior, since the flow regime is simply identified depending on the size of the drag coefficient with minimum and maximum functions. This approach is among others implemented in commercial codes like ANSYS Fluent and CFX. In this work, the latter approach is applied. Bubbly flow is set to occur when $C_{d,bubble} > C_{d,slug}$ and slug flow when $C_{d,slug} > C_{d,bubble}$. This functionality can be expressed as follows:

$$C_d = \max\left(C_{d,bubble}, C_{d,slug}\right) \tag{55}$$

For the virtual mass coefficient, a similar approach is taken to ensure continuity for this coefficient as well [34]:

$$C_{vm} = \min\left(C_{vm,bubble}, C_{vm,slug}\right) \tag{56}$$

It should be noted that these two formulation do not necessarily predict the same flow regime at the same time, however they ensure a stable convergence behavior that approximately captures the correct physics.

3.2.5. Material properties

The transport properties and equation of state for water in liquid and vapor state are accounted for using the IAPWS-IF97 database. This means that all properties are temperature dependent and some are pressure dependent. For oxygen, the equation of state is modeled using the ideal gas law. Similarly, temperature dependent properties are used that where extracted from Engineering Equation Solver (EES). The remaining parameters and relations of the PEMEC model are listed in table 2.

It should be noted that only the porosity and permeability of the PTL are measured. The specific pore surface area of the PTL is unknown. However, since the pore size resembles what is used for fuel cell applications, it can be expected to be in the order of 1.0×10^7 to $1.0 \times 10^8\,\mathrm{m}^2$ according to ref. [55]. Nonetheless, from a modeling point view the exact value is not important for two reasons. Firstly, in the model this parameter only affects heat transfer, and secondly, it results in a very high heat transfer rate between the phases, which essentially forces the fluid and solid phase temperatures equal. Moreover, this effect is already seen to occur at a specific surface area of $1.0 \times 10^6\,\mathrm{m}^2$, which means that there is no need for increasing the value further.

For the MPL some properties are taken from the literature, while others are calculated. The porosity of the MPL is calculated by taking the average porosity of the CL and MPL. This is meaningful since the backscattered electrons SEM images taken by [25] reveal that no clear interface exists between the layers. The porosity can be calculated as follows from the known material loadings, material densities and the combined thickness:

$$\varepsilon_{MPL} = 1 - \frac{\frac{m_{Nafion}}{\rho_{Nafion}} + \frac{m_{Ir}}{\rho_{Ir}} + \frac{m_{IrO_2}}{\rho_{IrO_2}}}{L_{MPL+CL}} \tag{57}$$

Where m is loading ($\mathrm{kg\ m^{-2}}$), and L_{MPL+CL} is the combined thickness.

For the permeability of the MPL, a value of $1.0 \times 10^{-13}\,\mathrm{m}^2$ is selected. This value is in agreement with measurements by Pant et al. [53] and Gurau et al. [56] for fuel cell applications. Moreover, it is in agreement with the applied values in other modeling studies of the CL and MPL [57, 58]. For the break through pressure of the MPL, which is needed in the van Genuchten model, a value of one order of magnitude higher than the PTL is specified. According to Gostick et al. [59], the break through pressure of a MPL for fuel cell applications can be two orders of magnitude larger than that of the PTL due to the small pore size. However, the numerical schemes in ANSYS CFX cannot handle so high values, hence the break through pressure is limited to being one order of magnitude larger.

3.3. Boundary conditions

The same boundary conditions as in our previous work (i.e. ref. [21]) are applied with respect to mass flows and temperatures at the inlet and outlet as well as capillary pressure at the PTL-channel interface. The adiabatic wall condition previously specified at the PTL-BPP interface has been moved to the CD-insulation interface.

To model contact resistance with respect to solid potential, the following formulation is applied:

$$\mathbf{n} \cdot (-\sigma \nabla \phi_s) = \frac{\phi_{s,BP} - \phi_{s,PTL}}{R_{c,p}} \tag{58}$$

Here $R_{c,p}$ is the contact resistances associated with electron transport across the interface or current constrictions ($\mathrm{m^2\ s\ kg^{-1}}$).

At the cathode-membrane interface, the membrane potential is set equal to zero, hence neglecting the overpotential associated with the hydrogen evolution reaction. Meanwhile, at the anode BPP boundary a uniform cell potential is applied:

$$\phi_{s,BP,wall} = V_{cell} \tag{59}$$

3.4. Numerical solution approach and mesh

The numerical model was developed and solved in the simulation framework of ANSYS CFX 18. The gas-liquid flow is solved using a coupled pressure, velocity and volume fraction solver. This type of solver is more computational demanding than a segregated solver; however it is necessary to avoid divergence during the iterative procedure. In order to couple the pressure and the velocities, a fourth order Rhie-Chow scheme is applied. This means that CFX applies a collocated grid; hence, all variables are stored in the same position. This applies also to additional scalar variables like electric potentials needed for modeling electrochemistry and charge transport.

For the remaining transport equations, a segregated solver is used in the solution procedure. This means that the species, turbulence, energy, and electric potential equations are solved one after the other in the listed order. To further stabilize the steady-state solver in CFX, a pseudo time-step is applied between 1×10^{-4} and 1×10^{-5} s. Moreover, all source terms are stabilized by providing the solver with the linearized source term.

For discretization of the advection terms in all conservation equations, the high resolution scheme is applied. The obtained discrete system of linearized algebraic equations, is then solved by applying an algebraic multigrid accelerated incomplete lower upper factorization technique.

To capture steep gradients in the volume fraction, the compressive interface capturing scheme for arbitrary meshes is activated. Here, a default slope limiter of 2 is specified.

This setting makes it possible to capture the very steep gradients that appear within the PTL and MPL while solving. Moreover, since a single domain formulation is used for the channel and porous media region, interface smoothing is carried out between the PTL and MPL using a hyperbolic function. This allows the solver too convergence more smoothly.

Each geometry consists of approximately 2.5 million cells. The 1.5 million cells located in the channels and porous media are hexahedron. The rest of the cells, which are found within the BPP, are triangular prisms.

To assess convergence of the developed model during the solution procedure, the residuals and the system imbalance of each transport equation is monitored, whilst the target residual is set to 1×10^{-6} and the imbalance is 1×10^{-1}. Furthermore, as an additional safety precaution, the minimum, maximum, average and standard deviation of the solved variables are monitored to ensure fully stable and converged results. The computational time at the investigated current density of $5\,\mathrm{A\,cm^{-2}}$ is one week, when applying 16 cores on a workstation with two Xeon CPU ES-2687W v3 (3.1 GHz) processors and 128 GB RAM memory. The computational time increases with decreasing mass flow. Thus, at $1\,\mathrm{A\,cm^{-2}}$, the computational time increases to 2-3 weeks.

3.5. Electrochemical parameter identification

To make sure the devised mathematical model can capture the electrochemical performance during high current density operation, the necessary electrochemical parameters for the OER (i.e. activation energy, exchange current density and apparent charge transfer coefficient) as well as the contact resistance are obtained by fitting a two-dimensional formulation of the devised model to measured polarization curves at four different temperatures.

The test cell by EWII Fuel Cells A/S, has an active area of 2.89 $\mathrm{cm^2}$. For the anode and cathode an interdigitated and parallel channel flow field is applied, respectively. Both the anode and cathode are operated at atmospheric conditions with a MEA compression of 2.3 MPa. The cell is operated at a constant water flow of 270 ml/min, which amounts to an excessive overstoichiometry of 35000 relative to a current density of 1 A $\mathrm{cm^{-2}}$. The high overstoichiometry operation ensures that the effect of temperature gradients and gas blockage in channels is minimized. The experimental setup applied is the same as in ref. [26].

The predicted polarization curves are obtained by running the developed model in two dimensions (2D) in the through-plane direction. Hence, in the fitting procedure, the model ignores channel flow, which is reasonable taken the high water stoichiometry into account. Moreover, the simulations are carried out in 2D, since a three-dimensional simulation of the full-scale PEMEC model takes approximately 1 to 3 weeks to compute with the available computational facilities. This computational time should be seen in strong contrast to the 2D simulations, which only take between 10 and 60 seconds per data point. In other words, for four polarization curves (or 24 data points) an unfeasible computational time of around a year is expected for the 3D model.

It should be noted that the 2D model also accounts for the cathode structure and the hydrogen evolution reaction (HER) to ensure that the fitted OER parameters do not include the behavior of the HER. To limit the number of unknowns in the fitting procedure, the apparent charge transfer coefficient and activation energy of the HER determined by Durst et al. [60] are applied. Moreover, the membrane water content is specified to 21, which approximately corresponds to a membrane compression of 2.3 MPa [24, 38]. This is furthermore in agreement with other modeling studies as shown in table 3.

In figure 5a, the predicted and measured polarization curves for 50 °C, 60 °C, 70 °C and 80 °C are shown for a current densities up to 5 A $\mathrm{cm^{-2}}$. For the depicted range in current density, the fitted model is able to predict the change in cell voltage for all temperatures. The activation region of the polarization curve is only visible at current densities less than 0.3 A $\mathrm{cm^{-2}}$. In the remaining part of the polarization curve the behavior appears linear, hence indicating that the change in cell potential is dominated by ion and electron transport losses. Nonetheless, a slight decrease in the slope is visible. From the model, it can be seen that this behavior is caused by a rising cell temperature, which lowers the ohmic resistance and activation losses. Generally speaking, this trend could also be caused by changes in the electrochemistry [44, 45, 26], however this is not included in the model. Finally, it should be noted that for the applied cell and operating conditions mass transport not a limiting factor. This trend is fully captured by the gas-liquid flow model and underlines the feasibility of the model.

The obtained electrochemical parameters are listed in table 3 alongside literature values. Moreover, a plot of the predicted overpotentials for 343 K are shown in figure 5b. From the conducted fitting, an apparent charge transfer coefficient in the anode direction of 1.375 is determined. This corresponds to a Tafel slope of 48 mV/dec at 333 K, which is slightly higher than the Tafel slope of 45 mV/dec determined from the high frequency resistance corrected Tafel plot analysis in ref. [26] for the same type of cell, compression and temperature. The main difference is due to the fact that the apparent charge transfer coefficient in this work is fitted across four temperatures, whilst in ref. [26] it is only determined for a single temperature. For comparison, refs. [61, 62] found the apparent charge transfer coefficient to be 1.4706 and 1.296, respectively, for a Pt – IrO_2 catalyst. These values correspond to Tafel slopes of 44.9 and 50.1 mV/dec, respectively, at a temperature of 333 K.

For the exchange current density, a value of $1.113 \times 10^{-3}\,\mathrm{A\,m^{-2}}$ at 333 K was determined in this work. Again for refs. [61, 62] at the same temperature, values of $1.02 \times 10^{-3}\,\mathrm{A\,m^{-2}}$ and $5.94 \times 10^{-3}\,\mathrm{A\,m^{-2}}$, respectively, were found. For both

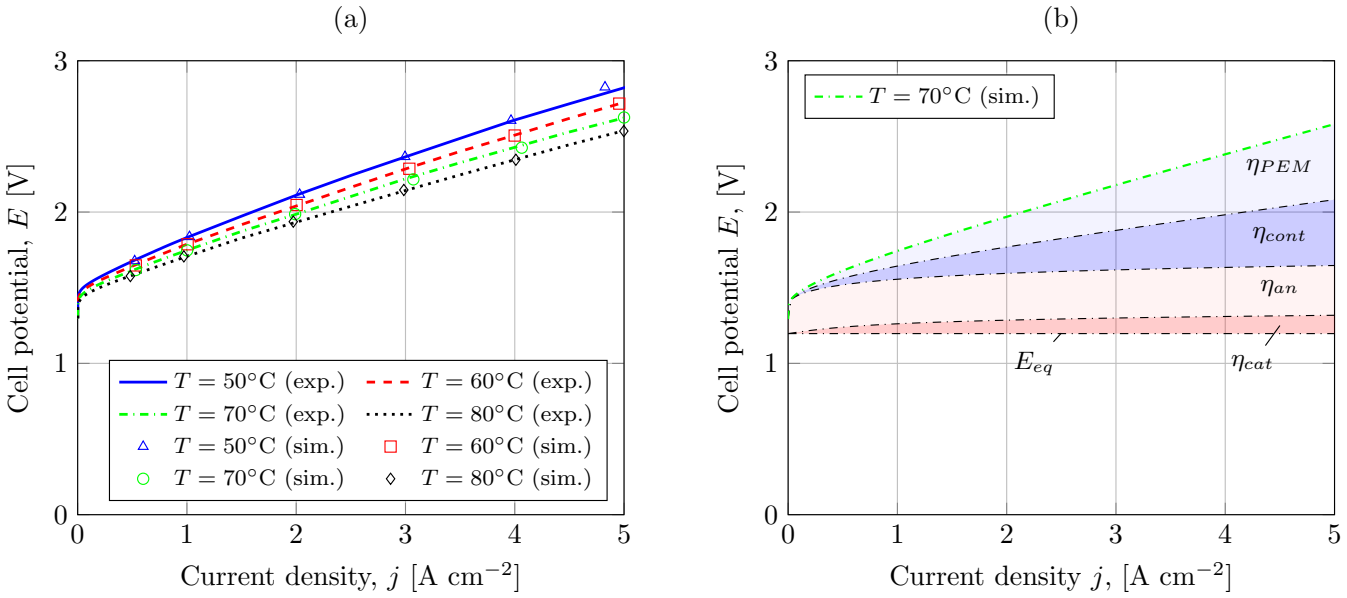

Figure 5: Polarization curves: (a) modeling fit vs. experimental measurements and (b) overpotential contributions at 343 K for an isothermal cell .

parameters, quite reasonable agreement is seen when comparing to literature values. However, when comparing the predicted activation energies, some differences appear. While our fitting determines a value of 73 kJ, refs. [61, 62] determine values of 53 kJ and 63 kJ, respectively. There can be several explanations for this difference. One explanation could be that studies in the literature neglect the cathode in their fitting procedures, which means that the activation energy of the OER has to compensate for any temperature effects of the HER. Another explanation could be that we are fitting our model over a much larger current density range then normally seen in the literature, and that we are including contact losses.

From the fitting procedure, we have also determined the total contact resistance of the cell to being $8.7 \times 10^{-6}\,\Omega\,\mathrm{m}^2$. This term includes all contacts losses and current constrictions in the CL. It should be noted that the large contact resistance for this specific cell is due to poor contact between the BPP and CD at the anode and cathode, as shown by Frensch et al. [26] from ex-situ measurements. Hence, for a stack this contribution will be significantly less compared to a single cell. When further comparing the fitted contact resistance to the ex-situ measured contact resistance of $4.3 \times 10^{-6}\,\Omega\,\mathrm{m}^2$, a substantial difference is seen. One explanation for this discrepancy is the electrical resistance that occurs due to current constrictions in the CL as discussed by Elsøe et al. [25]. For the same type of cell as studied in this work, the authors determined that the non-membrane ohmic losses accounted for approximately 55 %. From figure 5b it can be seen that our fitting predicts that non-membrane ohmic losses account for 47 %. Thus, the determined contact resistance seems reasonable.

Finally, it should be noted from figure 5b that the cathode overpotential only contributes with 10 % to the total overpotential loss of the cell at a current density of $5\,\mathrm{A\,cm}^{-2}$. Hence, in order to reduce modeling requirements, it is acceptable to neglected the cathode in the three-dimensional case study presented in the following. Moreover, it can be noted that when approaching a current density of $5\,\mathrm{A\,cm}^{-2}$, the overpotential losses due to ion transport in the PEM, contact resistance and anode kinetics are approximately equal in share. Hence, performance at higher current densities can be greatly improved by mainly addressing contact losses or reducing the thickness of the PEM. Obviously, decreasing PEM thickness increases hydrogen cross-over and the hydrogen to oxygen ratio. However, the hydrogen to oxygen ratio is adversely affected by an increasing current density [64]. Thus, it may still be feasible to apply a thinner membrane as long as the risk of pin holes is low enough.

4. Results and discussion

4.1. Overall performance comparison

The main purpose of investigating flow field designs is to improve the understanding of which design parameters affect the distribution of heat and mass in relation to electrochemistry. To assess the overall performance of the three investigated cases, the cell potential and pressure losses as well as statistical properties of the ion current density, gas volume fraction and temperature fields are evaluated in table 4.

Firstly, it should be noticed that the cell potential is virtually the same for all three cases. With this in mind, it could appear that there is no significant difference between

Reference	This work	[61]	[62]	[63]
Year of publication	2018	2018	2015	2015
Anode catalyst	Ir – IrO_2	Pt – IrO_2	Pt – IrO_2	Pt – IrO_2
Apparent charge transfer coefficient α_{an}	1.375	1.471	1.296	0.8
Exchange current density $j_{0,a}$ / $\mathrm{A\,m^{-2}}$	$2.348\,39 \times 10^{-4a}$	1.22×10^{-4a}	$\left[1.1 \times 10^{-3}, 2.4 \times 10^{-2}\right]$	1×10^{-3d}
Activation energy $E_{act,a}$ / kJ	72.997	52.994	62.836	-
Cathode catalyst	Pt/C	Pt	Pt	Pt
Apparent charge transfer coefficient α_{an}	0.5^{b}	-	-	0.25
Exchange current density $j_{0,a}$ / $\mathrm{A\,m^{-2}}$	1.65×10^{3a}	-	-	1×10^{-3d}
Activation energy $E_{act,a}$ / kJ	16^{b}	-	-	-
PEM	Nafion 117	Nafion 117	Nafion 117	Nafion 117
Water content	21	-	16	21
Total contact resistance R_c / $\Omega\,\mathrm{m^2}$	8.7e-6	-	-	-

Table 3: Electrochemical parameters. [a]The exchange current density determined relative to a reference temperature of 298.15 K.[b]The charge transfer coefficient and activation energy was measured experimentally by Durst et al. [60]. [c]The water content is predicted by taking the compression into account according to Kusoglu et al. [38]. [d]It is unclear at what reference temperature the values where obtained.

Case	Cell potential V	Pressure loss kPa	Ion current density $\mathrm{A\,cm^{-1}}$			Temperature K			Gas volume fraction		
			Mean	Max	STD	Mean	Max	STD	Mean	Max	STD
A	2.66	59.936	5	5.50	0.200	349.3	360.3	4.62	0.288	0.477	0.098
B	2.67	60.162	5	5.62	0.204	349.3	361.6	4.60	0.285	0.597	0.092
C	2.65	68.315	5	5.80	0.220	349.5	363.4	3.61	0.279	0.662	0.097

Table 4: Variables and statistical parameters. The ion current density and temperature field are evaluated in the PEM and the gas volume fraction field in the PTL.

the three design cases. Regardless, important differences are revealed from other parameters. In particular, issues that can affect degradation.

In terms of pressure loss, Case A and B behave very similar. Indeed, only a slight increase is seen from Case A to B. However, when comparing Case C to A and B, a substantial increase in pressure loss of 14 % is observed. This increased pressure loss for Case C is related to the gas volume fraction distribution within the channels and PTL. Particularly within the PTL, the relative permeability of the liquid phase exhibits a strong power law dependence on the gas volume fraction according to the van Genuchten relationship. Consequently, the pressure loss through the PTL is highly sensitive towards changes in the local gas volume fraction.

While the mean value of the gas volume fraction field is nearly the same for all three cases, the maximum and standard deviation increase from Case A to C. From a design point of view, these changes indicate that the introduction of equal land area as well as bended channels increase the gas maldistribution within the PTL. From a further comparison of Case A and B, it can be seen that even though the mean and standard deviation decrease when applying equal land areas between channels, the increase in maximum value counter balances this effect.

For the temperature fields within the PEM, a similar behavior as for the gas volume fraction is seen. In all three cases, the mean values are approximately the same, i.e. 3 K above the set point for the outlet temperature. As opposed to the gas volume fraction, the standard deviation values are the same for the three temperature fields. Despite that both the mean and standard deviations are virtually the same, the maximum temperatures are very different. In fact, substantial deviations from the intended operating temperature of 343.15 K are seen. For Case A, B and C, the maximum temperatures are 17.2, 18.4 and

20.2 K higher than the set point of the outlet, respectively.

Now that the statistical properties of the gas volume fraction and temperature fields have been discussed, the ion current density fields are addressed. Between the three cases, a large variation in the maximum current density is found. This pattern corresponds to what is found for the gas volume fraction and temperature fields. Moreover, the largest contrast is found between Case A and C, where a difference of 0.3 $\mathrm{A\,cm^{-1}}$ in maximum current density exists. In spite of these large deviations from the mean value, only minor differences are found between the standard deviation for all cases.

To clarify the cause of the overall differences, the flow fields for each case is examined in detail in the following.

4.2. Heat and mass maldistribution between channels

To evaluate the direct impact of a flow field design on mass and heat transport, the distribution between channels is analyzed. For doing so, two parameters are introduced: the normalized channel mass quality and the temperature difference between the interdigitated channels and the outlet.

The mass quality of a gas-liquid flow in a channel is defined as the mass flux of the gas phase relative to the total mass flux:

$$\chi = \frac{G_g}{G_g + G_l} \tag{60}$$

$$G_i = \frac{1}{A_c} \int_{A_c} \rho_i \mathbf{u}_i \cdot \mathbf{n} dA \tag{61}$$

Here G is the mass flux ($\mathrm{kg\,m^{-2}\,s^{-1}}$), A_c is the cross-sectional area of the channel and $\mathbf{n}$ is the normal vector to the cross-sectional area. Mass quality is an interesting parameter to examine, since it reveals how well the liquid water is distributed relative to where the gaseous oxygen is being produced and heat is released in the electrochemical reactions. To make the interpretation of the mass quality for the gas-liquid flow exiting each interdigitated channel easier, it is normalized by the mass quality of the gas-liquid flow at the outlet of the cell:

$$\chi_i^* = \frac{\chi_i}{\chi_{out}} \tag{62}$$

Here the subscripts i and *out* indicate channel number and total flow out, respectively. In the calculation of the mass fluxes, a cross-section area a few millimeters before the manifold is selected.

In figure 6a the normalized mass quality of the gas-liquid flow exiting each interdigitated channel of the cell is shown. When comparing the mass quality distributions, large differences can be seen. While Case A exhibits an unsymmetrical and parabolic distribution, Case B and C both depict a linear variation. The most predominant differences in mass quality are found for channel 1 and 2. Here Case A receives significantly more water then intended, while the diametrically opposite appears for Case B and C.

The mass flow weighted temperatures out of each channel can be seen in figure 6b. Overall, no extreme variation is observed between the fluid temperatures in each channel. The maximum undershoot is barely above 2 K, while the maximum overshoot is less than 2 K. When comparing the cases, temperature variations corresponding to the mass quality distribution can be seen. At the locations where the mass quality is low, the lowest temperatures are also found. This applies for example for channel 1 in Case A and channel 6 in Case B and C. The opposite trend is similarly visible, where mass quality is highest, i.e. channel 1 and 2 in Case B and C.

4.3. In-plane variations of two-phase flow in channels and PTL

The gas volume fraction distribution within the channel structure is depicted in figure 7. When comparing figure 7 to figure 6a, similar distributions between the channels can be observed for all three cases. This tendency is particularly evident, when examining channel 1 and 2 for Case A and B. For these channels, the same large difference is clearly visible.

A further examination of the gas volume fraction distribution reveals that the model predicts that the gas phase enters the inlet channels and to some extent prevents the free flow of the liquid phase to the PTL. This predicted behavior is in good agreement with experimental observations from *ex-situ* visualization studies of the interdigitated anode flow field for PEMEC conducted by Lafmejani et al. [65]. Another phenomenon to notice is the occurrence of flow separation in the manifold, where the flow from all the interdigitated channels merge. Here the gas phase appears to be caught in re-circulation zones near the sharp corners. A consequence of this behavior is an increased pressure loss. This behavior could be mitigated by applying fillets to the sharp corners.

From the gas-liquid flow within the interdigitated channel structure a direct link can be established to the flow within the PTL. In figure 8 the distribution of the gas volume fraction within the PTL is depicted. First, the effect of switching from Case A to B should be noticed. While the highest gas volume fractions for Case A is observed underneath the land area between the longest channels, i.e. channel 5 and 6, the highest gas volume fraction for Case B is found between the shortest channels, i.e. channel 1 and 2. Thus, the maldistribution of mass between the channels is clearly linked to the distribution within the PTL. Second, it should be noticed for Case A and B that gas tends to accumulate under the outlet channels and in particular halfway along the length of the channels. As already discussed in ref. [21], this distribution effect can be mitigated by curving channels, whereby a more even velocity field within the PTL is obtained. Nevertheless, if the channels are curved too much, the gas accumulation

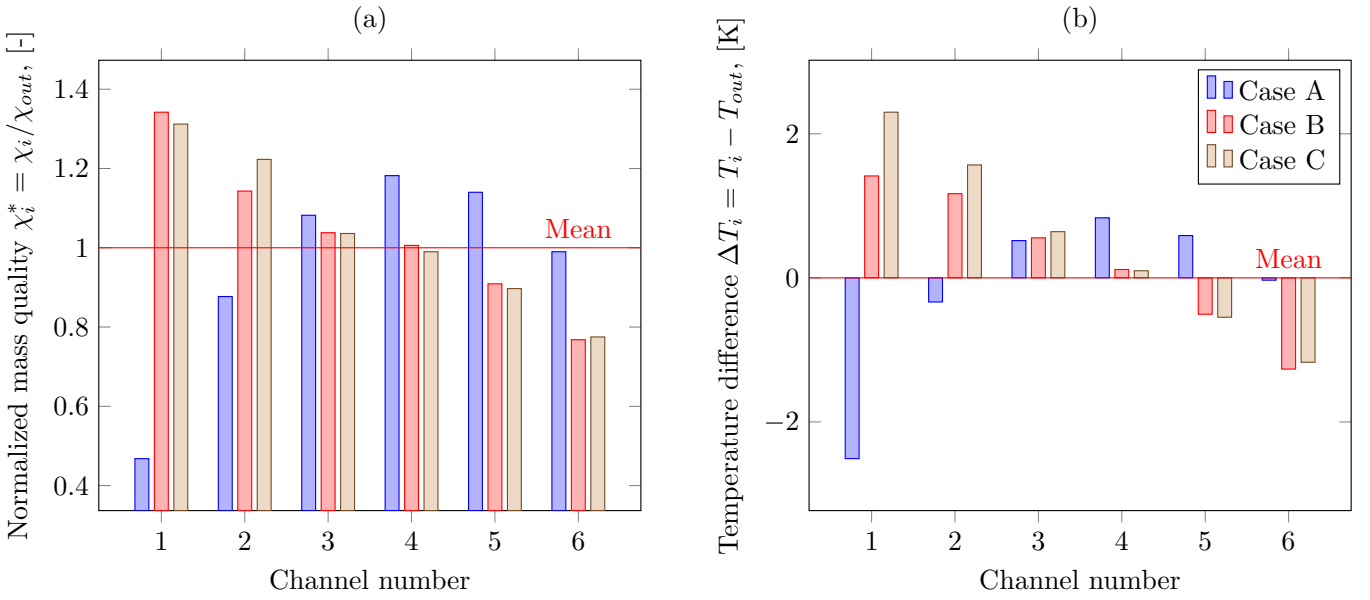

Figure 6: Maldistribution among outgoing interdigitated channels: (a) channel mass quality normalized by the outlet mass quality $x_{out} = 0.00267542$ and (b) temperature difference between channel and outlet.

zone is move from half-way in the channel direction to the beginning of the channels. This effect can clearly be seen when comparing Case A and B against C. Here bending of the channels creates severe gas hold up underneath of channel 2, 3 and 4 near the beginning of the outgoing channels. The observed trend of gas hold up underneath the outgoing channels has previously been shown experimentally for square, interdigitated flow fields in fuel cells[66].

When keeping in mind that the Euler-Euler model only gives an averaged representation of the gas volume fraction distribution, it is likely that areas of high gas volume fractions could lead to stagnant gas similarly as is observed experimentally by Selamet et al. [12]. Hence, it could be imagined that even more severe hot spot formations would be observable experimentally.

The distribution of the liquid phase superficial velocity magnitude within the PTL is depicted in figure 9. One of the main reasons for bending the interdigitated channels in Case C is that for straight channels the velocity profile along the length of the channels underneath the land area is parabolic shaped with the highest velocities near the beginning and end of the channels. This trend is clearly seen from observing Case A and B. By then bending the channels, the velocities along the length of the channels become more uniformly distributed as seen in case C. A further comparison between Case A and B reveals that switching from an equal spacing between channels to an equal land area size, forces lower velocities between the smallest channels as intended. For both Case A and B, small zones with very low liquid phase velocities arise between the shortest channels as highlighted in the figure. For Case C a large zone of lower liquid superficial velocities appears near the beginning of the channels. This zone coincides with the location of high gas volume fraction. Thus, the high extent of gas holdup appears to reduce the flow of the liquid phase.

To study the gas volume fraction fields in more detail, the variations in the channel and through-plane direction for channel 6 are plotted in figure 10a and 10b, respectively. For the distribution in the channel direction, i.e. figure 10a, an initial rapid increase is seen for all case. However, from here on Case C stands out. While the gas volume fraction for Case A and B keeps increasing along the length of the channel, the opposite trend occurs for Case C. Indeed, after the initial rapid increase, the gas volume fraction begins to decrease and finally reaches the same gas volume fraction as Case B. The observed distribution for Case C is caused by the curved shape of the neighboring channel, which makes the land area widest in the beginning and in the end of the channel. Hence, more gas relative to liquid is forced through in the beginning of the channel, which results in the observed distribution. When comparing the overall trend of Case A and B to the experimental observations by Hoeh et al. [16], a good agreement is observed. In their measurement of the time-averaged, gas volume fraction along the length of a channel in the anode of PEMEC, the same range of gas volume fractions in the channel is visible. Although Hoeh et al. [16] applies an serpentine flow field,

In figure 10b the through-plane distribution of the gas volume fraction across the channel, PTL and MPL is depicted. For the investigated location, it is evident that only minor variations in the gas volume fraction arise in the through-plane direction within each layer. The predominant change in gas volume fraction is observed at the channel-PTL and PTL-MPL interface. Particular, the

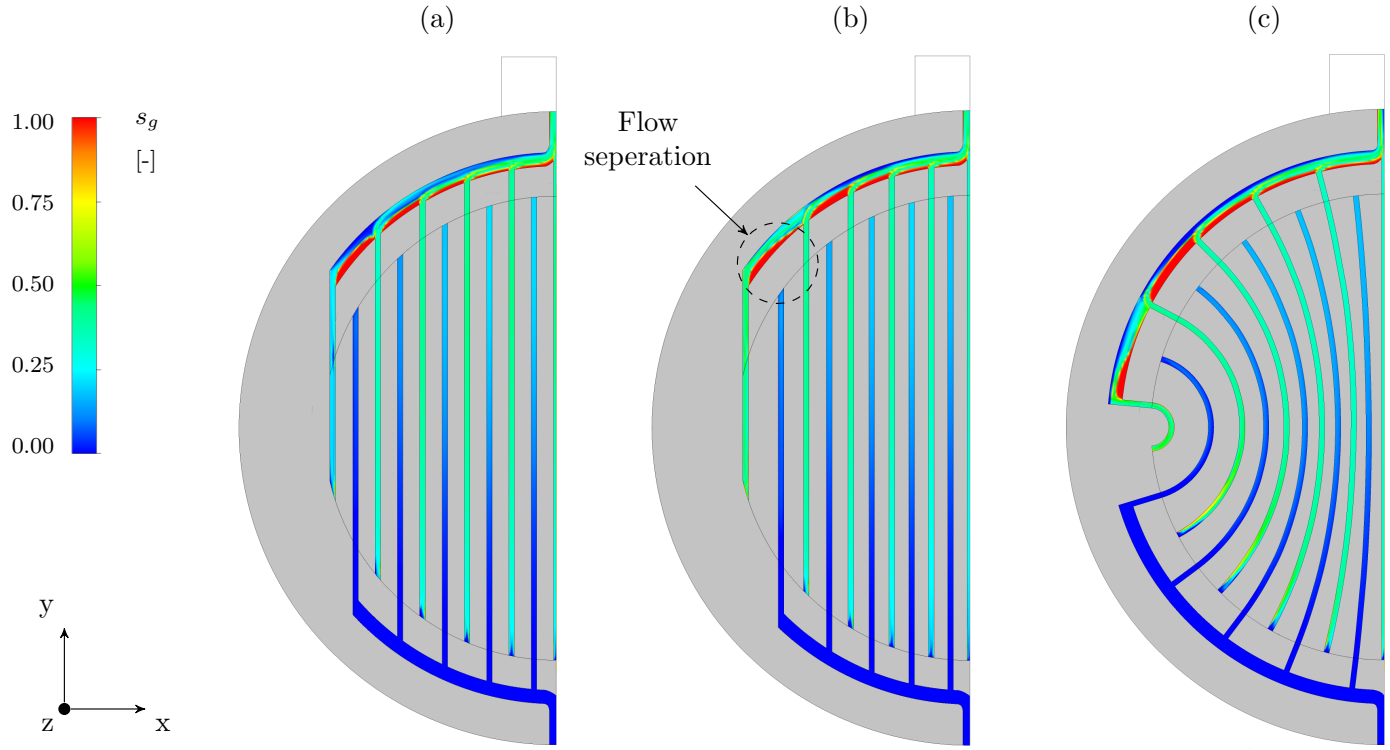

Figure 7: In-plane distribution of gas volume fraction for Case A, B and C, respectively, mid-way in the through-plane direction of the channels.

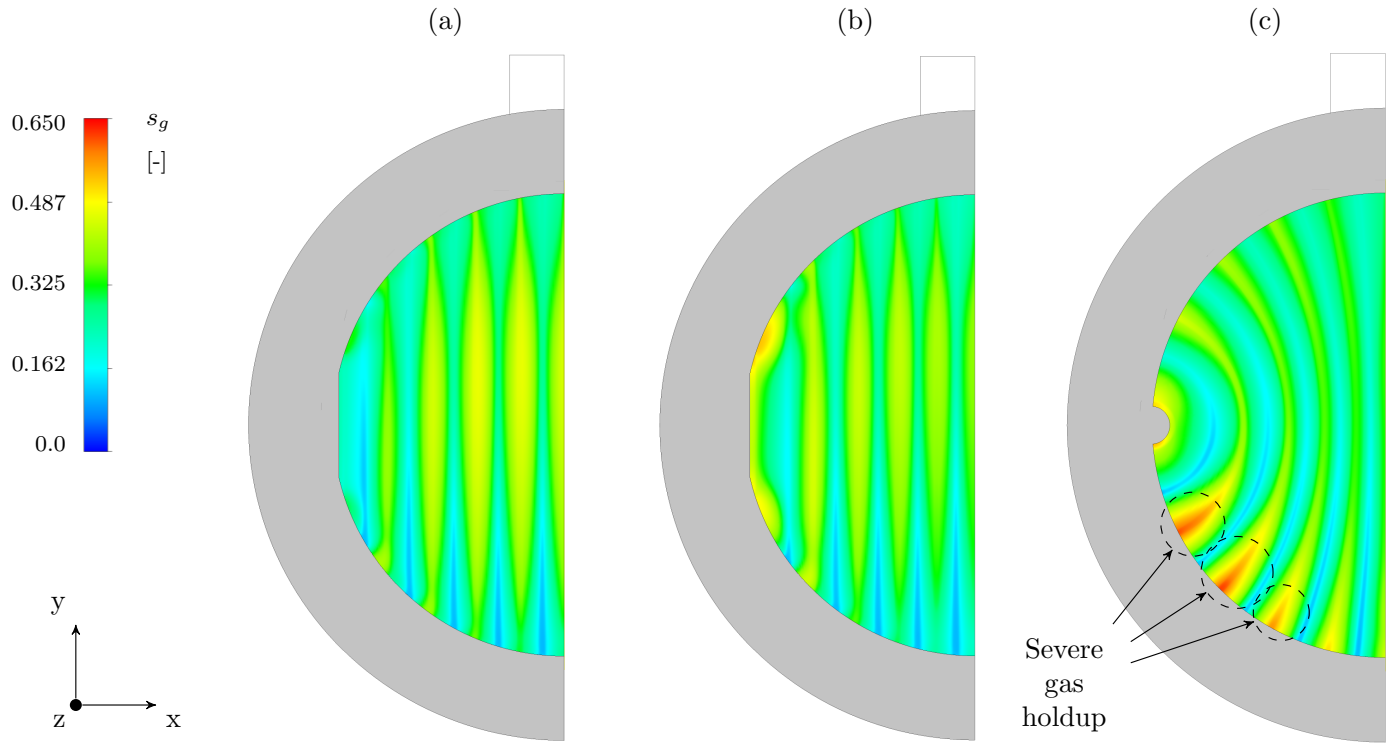

Figure 8: In-plane distribution of gas volume fraction mid-way in the through-plane direction of the PTL for Case A, B and C, respectively. It should be noted that the maximum gas volume fraction on the scale is limited to 0.75 in order to make differences more visible.

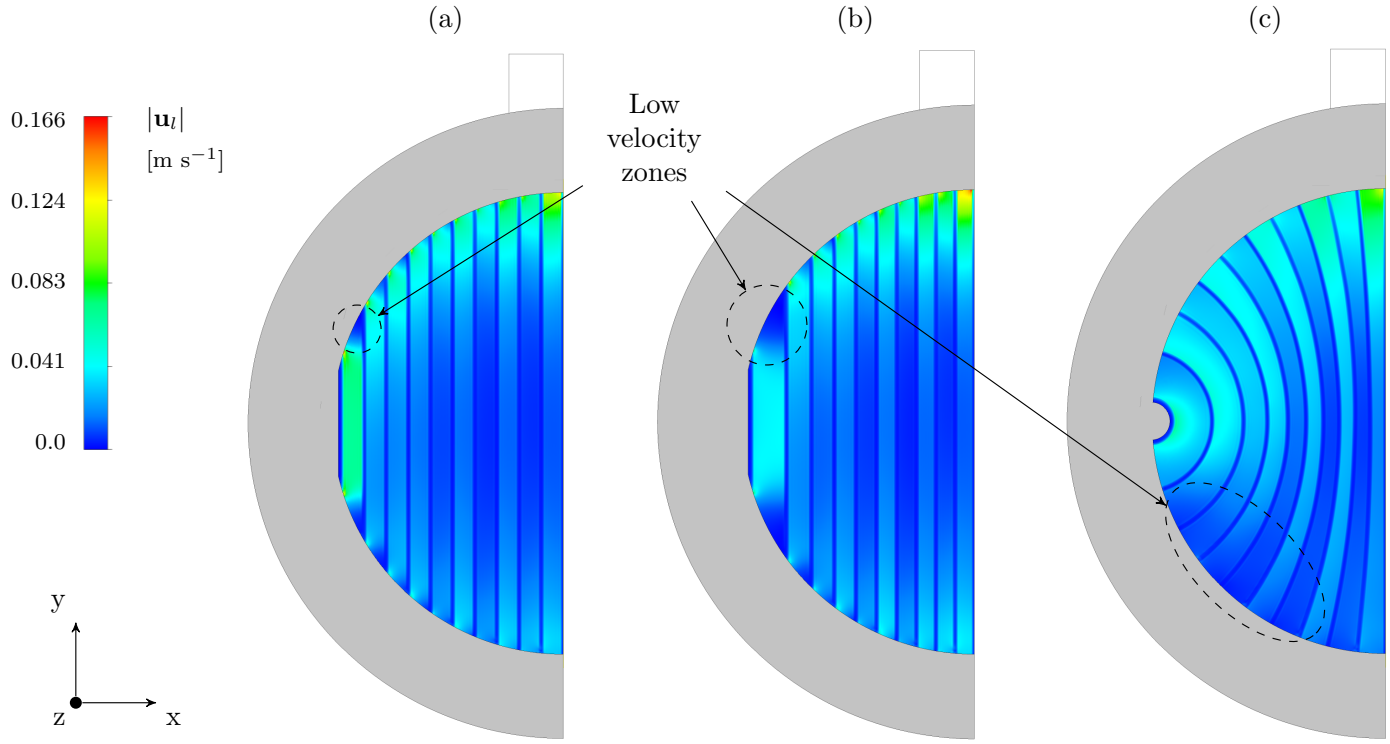

Figure 9: In-plane distribution of the liquid phase superficial velocity mid-way in the through-plane direction of the PTL for Case A, B and C, respectively.

discontinuity at the PTL-MPL interface is a well-known phenomenon that occurs when two porous media with different material properties are in direct contact[52, 67, 57].

When examining the gas volume fraction distribution across the MPL, two things should be noticed. There is no apparent difference between the three cases and the gas volume fraction is significantly lower than in the channel and PTL. This observation for the MPL may seem odd. Nonetheless, this difference in behavior can be be explained by the fact that the MPL consists of hydrophilic micro-pores that exert a large capillary force onto the gas bubbles and hence pushes them out of the layer. An implication of the applied MPL is thus that mass transport of the liquid phase towards the CL is significantly improved. In other words, the MPL sucks in the available water and secures that mass transport losses are avoided at high current density operation as has been shown experimentally by Lettenmeier et al. [68].

4.4. In-plane variations of heat and charge in PEM

The movement of charge, heat and mass are directly coupled. On one hand, the electrochemistry depends on temperature and the access of liquid water, and on the other hand, ion transport within the PEM is temperature dependent. To investigate the maldistribution of heat, the in-plane temperature distribution half-way through the PEM is depicted as a contour plot in figure 11.

The simulation results show that hot spots tend to form under the outlet channels and in particular half-way along the length of the channels for Case A and B, whereas for Case C in the beginning of the channels. Thus, curving the channels eliminates the formation of hot spots half-way in the channel direction, however it may cause even larger hot spot areas in the beginning of channels. The occurrence of hot spots furthermore coincide with the regions where the liquid phase has the lowest superficial velocity, hence where convective cooling is worst.

In figure 12, the in-plane current density distribution half-way through the PEM is shown as a contour plot. For all three ion current density fields, a fairly non-uniform distribution is seen. The lowest ion current densities are found under the inlet channels, where the temperatures are lowest. Correspondingly, the largest ion current densities are found underneath the outlet channels, where the temperatures are highest. High ion current density regions coincide with the occurrence of hot spots within the PEM, which should be avoided, since the irreversible degradation of the PEM is directly linked to the occurrence of high temperatures [69]. As discussed by Bauer et al. [70], when the temperature reaches 363 K, the risk of both thermal and mechanical degradation of Nafion membranes increases substantially due to the low glass transition temperature. Another degradation phenomena that is related to hot spots, as pointed out by Nandjou et al. [71], is the increased hydrogen permeation that can cause local damage of Nafion.

In terms of modeling approach, the large variations

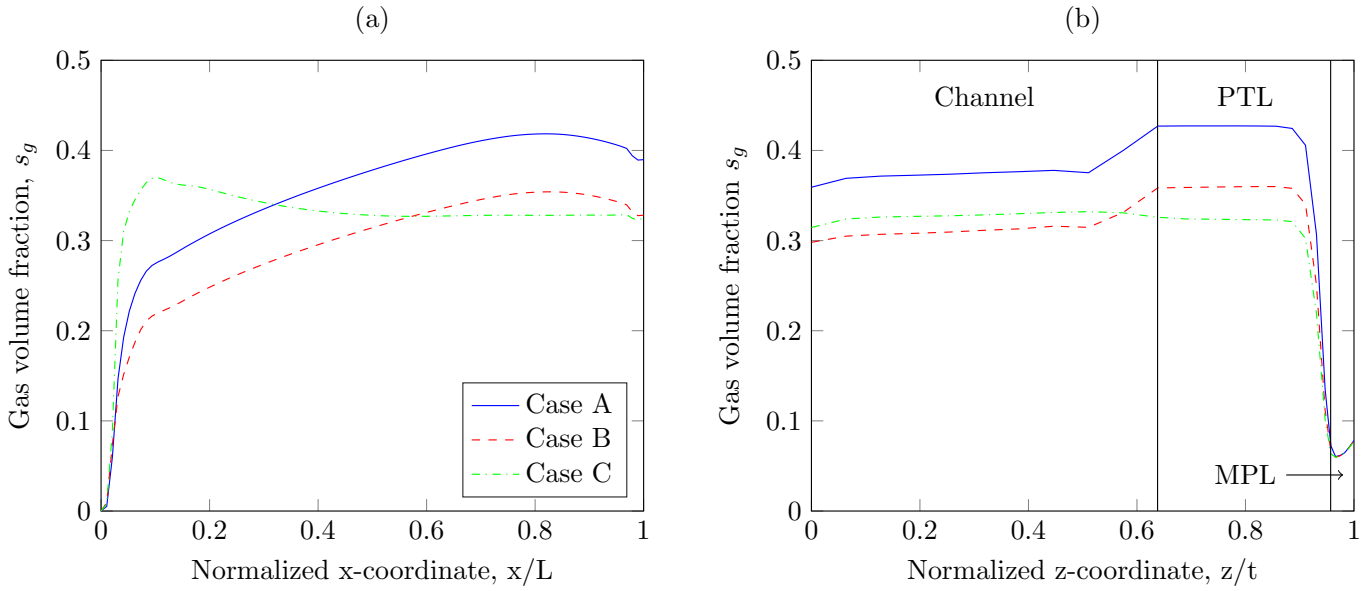

Figure 10: Gas volume fraction distribution: (a) along the channel direction and (b) through-plane direction, mid-way in channel 6.

in temperature and ion current density underline the importance of including detailed electrochemistry and charge transport phenomena for modeling high current density operation. Moreover, it makes the approach of simply applying a uniform current density distribution questionable and should hence be avoided. Specifically in regard to modeling of the temperature field, it should furthermore be noted that cooling occurs best in the areas nearest the BPP, the inlet manifold and the inlet channels. Hence, including the BPP is highly important in predicting the occurrence of hot spots near the perimeter of the cell as truthfully as possible.

5. Conclusion

The three-dimensional PEMEC model developed in this work is the most comprehensive to date. The model enables the simulation of full-scale cells at current densities of up to $5\,\mathrm{A\,cm^{-2}}$ with a higher accuracy then previously seen. The motivation behind this research effort has been two-folded. On one hand, it was desired to strengthen the accuracy of the model presented previously in ref. [21]. On the other hand, it was of interest to evaluate the feasibility of applying a state-of-the-art high pressure PEMEC with a circular, interdigitated anode flow field for high current density operation.

The presented PEMEC model has been improved by adding charge transport and electrochemistry, detailed momentum transfer terms that reflect the possible two-phase flow patterns, phase change as well as the jump-condition at the domain interface between the PTL and MPL due to capillary pressure. Of these, in particular capillary pressure and phase change are not trivial tasks to implement in a three-dimensional modeling framework with material properties that are temperature and pressure dependent as seen when applying the IAPWS-IF97 database for water in liquid and vapor state.

In order to acquire the needed electrochemical parameters to match the performance of a state-of-the-art PEMEC from EWII Fuel Cell A/S, a two-dimensional formulation of the developed model was fitted to polarization curves for four different temperatures. It was found that the obtained parameters are in good agreement with values found in the literature and that the cathode overpotential contributes to only 10 % of the total overpotential at a current density of $5\,\mathrm{A\,cm^{-2}}$. Moreover, the contribution due to anode kinetics, ion transport in the PEM and the lumped contact losses are equal in share for the investigated cell. Hence, cell performance at higher current densities is easiest improved by addressing contact losses or reducing membrane thickness.

To investigate the high current density operation of a PEMEC, three different designs for circular, interdigitated flow fields suitable for asymmetric high pressure operation are investigated in terms of their ability to ensure an uniform distribution of charge, heat and mass throughout the critical parts of a PEM electrolysis cell. The following list summarizes the major conclusions from the case study:

- A model has been developed that is capable of accurately predicting the polarization curves of a PEM electrolysis cell over a large current densities and for temperatures between 323 and 353 K.

- Operating a state-of-the-art PEM electrolysis cell with an interdigitated flow field at approximately $5\,\mathrm{A\,cm^{-2}}$ for a water stoichiometry of 350, causes a large in-plane variation in the local ion current density of up to $1.5\,\mathrm{A\,cm^{-2}}$ and in the local temperature

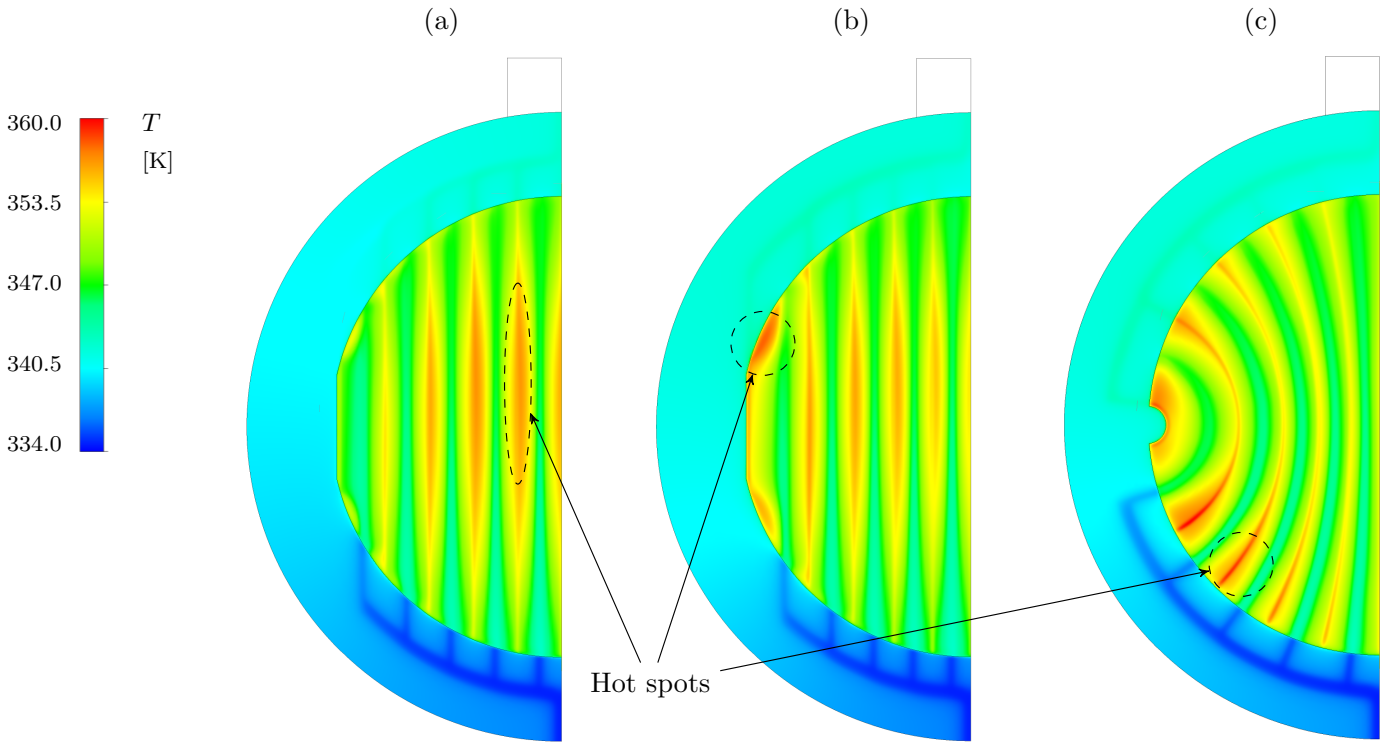

Figure 11: In-plane distribution of temperature for Case A, B and C, respectively, mid-way through the PEM and gasket.

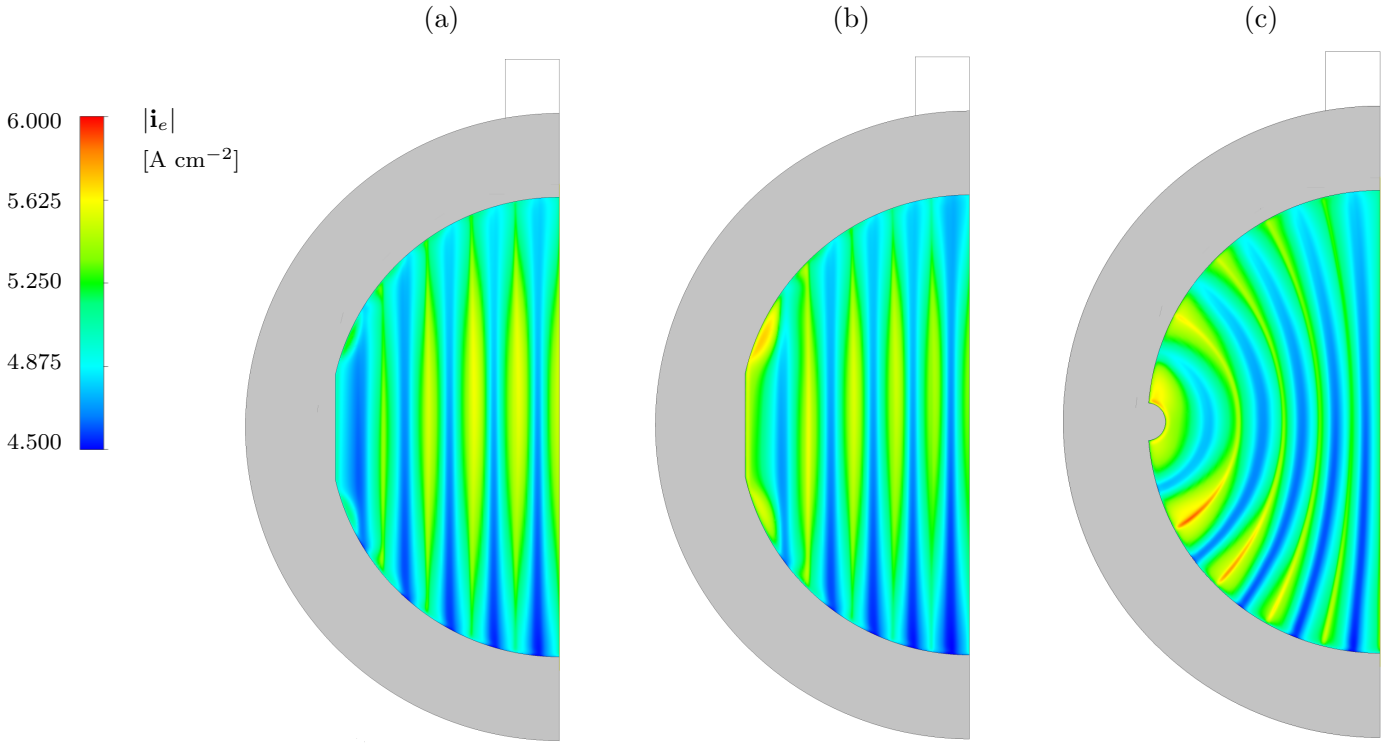

Figure 12: In-plane distribution of current density variation for Case A, B and C, respectively, mid-way through the PEM.

of up to 20.2 K above the intended cell temperature.

- Although the investigated cases cause in-plane variations in temperature that can lead to irreversible degradation of the PEM, the overall electrochemical performance in terms of cell voltage and cell current density is not affected by the specific interdigitated anode flow field. Hence, one should be careful when solely judging a cell design from the electrochemical performance.

- For the three studied designs, the flow field with equal land width between channels (i.e. Case A) gives the most uniform distribution of temperature and ion current density, although minor hot spots still appear. Because degradation is known from literature to be adversely affected by the formation of hot spots, higher water stoichiometries or an flow field with thinner land area width is recommended for high current density operation of an asymmetrically pressurized PEMEC. Moreover, it would appear that an improved design could be obtained by having an uneven distribution land area width as well as applying a slight bend of the channels. However, a such attempt should be undertaken with much care. Obviously, it is easy to decrease the land area width, however the extent of this depends on the mechanical properties of the BPP due to the stresses that are imposed by the asymmetric pressurization.

- The locations of high current densities coincide with the locations of a high gas volume fractions and a high temperatures. Hence, capturing the coupling of these phenomena is essential in obtaining the highest accuracy.

- By incorporating phase change as well as the presence of the BPP in the modeling, it is found that hot spots near the perimeter of the cell are greatly reduced.

For now, the main focus of the conducted research effort has been on ensuring that the accuracy of the required closure equations and the accuracy of the parameters needed for modeling the electrochemical performance for high current density operation. Hence, extensive efforts are still needed to further validate the predictions of the gas volume fraction, temperature and current density fields. For doing so, not only a single method can be applied. While the temperature and current density fields can be obtained using a segmented cell, the gas volume fraction within the channels can either be measured *in-situ* using optical visualization or neutron radiography. Our first attempts in ref. [65, 15] to visualize the gas-liquid flow *ex-situ* in the channels have given information about the approximate bubble sizes and flow regimes. In the next step, the local gas volume fractions and bubble sizes within the channels are going to be obtained *in-situ*. This data can can then be used for validating the presented two-fluid and the VOF model in ref. [23].

Acknowledgments

This work was supported by the Innovation Fund Denmark through the e-STORE project (J.No. 4106-00025B). The authors would in addition like to thank EWII Fuel Cell A/S for supplying the single cell for measuring the polarization curves.

Nomenclature

Greek letters

λ	Water stoichiometric coefficient	-
ρ	Density	$\mathrm{kg\,m^{-3}}$
ε	Volume porosity	-
τ	Viscous shear stress	Pa
Γ	Volume specific mass flow rate	$\mathrm{kg\,s^{-1}\,m^{-3}}$
Γ	Molecular diffusion coefficient	$\mathrm{kg\,s^{-1}\,m^{-1}}$
μ	Dynamic viscosity	$\mathrm{Pa\,s}$
σ	Electron conductivity of the solid phase	$\mathrm{S\,m^{-1}}$
κ	Ion conductivity of the electrolyte phase	$\mathrm{S\,m^{-1}}$
ϕ	Electrostatic potential	V
ω	Turbulent eddy dissipation frequency	$\mathrm{s^{-1}}$
α	Apparent transfer coefficient	-
β	Symmetry factor of the rate determining step	-
χ	Mass quality	-

Sub- and superscripts

g	Gas phase
l	Liquid phase
m	Mixture
i	Species i
out	Outlet
s	Solid phase
e	Electrolyte phase
c	Capillary
c	Contact
d	Drag
b	Before the rate determining step
a	After the rate determining step
rds	Rate determining step
eq	Equilibrium
vm	Virtual mass
sat	Saturation
ec	Electrochemical reactions
T	Turbulence
D	Dispersion
pm	Porous media
p	Pore
eff	Effective properties
H_2O	Water
O_2	Oxygen
mass	Mass transfer

Latin letters

x	Mole fraction	-	Y	Mass fraction	-
p	Partial pressure	Pa	$\mathbf{J}$	Diffusion mass flux relative to a mass-averaged velocity	$\mathrm{kg\,s^{-1}\,m^{-2}}$
P	Pressure	Pa	D	Diffusion coefficient	$\mathrm{m^2\,s^{-1}}$
P	Turbulence production due to buoyancy	$\mathrm{m^2\,s^{-2}}$	d	Characteristic diameter	m
I	Current	A	Re	Reynolds number	
j	Current density	$\mathrm{A\,m^{-2}}$	Sc	Schmidt number	-
$\mathbf{i}$	Current density vector	$\mathrm{A\,m^{-2}}$	Pr	Prandtl number	-
L	Length	m	Sh	Sherwood number	-
$\dot{m}$	Mass flow	$\mathrm{kg\,s^{-1}}$	R	Reaction rate	$\mathrm{A\,m^{-3}}$
G	Mass flux	$\mathrm{kg\,s^{-1}\,m^{-2}}$	R	Universal gas constant = 8.314472	$\mathrm{J\,K^{-1}\,mol^{-1}}$
m	Mass loading	$\mathrm{kg\,m^{-2}}$	R	Electrical resistance	$\mathrm{m^2\,s\,kg^{-1}}$
M	Molecular weight	$\mathrm{kg\,kmol^{-1}}$	T	Temperature	K
F	Faraday's constant	$\mathrm{C\,mol^{-1}}$	e	Internal energy	J
N	Number of entities	-	h	Enthalpy	J
A	Area	$\mathrm{m^2}$	h	Mass convection number	$\mathrm{m\,s^{-1}}$
a	Specific interfacial area	$\mathrm{m^{-1}}$	k	Thermal conductivity	$\mathrm{W\,m^{-1}\,K^{-1}}$
$\mathbf{u}$	Superficial velocity vector	$\mathrm{m\,s^{-1}}$	k	Turbulent kinetic energy	$\mathrm{m^2\,s^{-2}}$
$\mathbf{U}$	True velocity vector	$\mathrm{m\,s^{-1}}$	Q	Heat dissipation	$\mathrm{W\,m^{-3}}$
s	Saturation	-	E	Electric potential of an electrode relative to reference electrode	V
$\mathbf{g}$	Gravity vector	$\mathrm{m\,s^{-2}}$	$\overline{V}$	Molar volume	$\mathrm{m^3\,mol^{-1}}$
$\mathbf{M}$	Interfacial momentum transfer	$\mathrm{kg\,m^{-2}\,s^{-2}}$	v	Stoichiometric factor, i..e. the number of times the rds has to occur for the overall reaction to take place once	
$\mathbf{n}$	Normal vector	-	n	Number of electrons transfered	-
K	Viscous permeability	$\mathrm{m^2}$	C	Dimensionless coefficient	-
k_{rel}	Relative permeability	-	EW	Equivalent weight of Nafion	$\mathrm{kg\,mol^{-1}}$

References

[1] M. Carmo, D. L. Fritz, J. Mergel, D. Stolten, A comprehensive review on PEM water electrolysis, International Journal of Hydrogen Energy 38 (12) (2013) 4901–4934, ISSN 03603199, doi:10.1016/j.ijhydene.2013.01.151.

[2] P. Sanchis, M. Ieee, Water Electrolysis : Current Status and Future Trends 100 (2).

[3] H. Xu, G. Inc., Benchmarking Catalyst Activity and Durability for Water Electrolysis, in: The 1st International Conference on Electrolysis, 2017.

[4] E. B. Anderson, Proton OnSite, Advancing PEM Electrolysis for Current and Future Hydrogen Markets, in: The 1st International Conference on Electrolysis, 2017.

[5] K. A. Lewinskia, D. F. van der Vlieta, S. M. Luopaa, NSTF Advances for PEM Electrolysis - The Effect of Alloying on Activity of NSTF Electrolyzer Catalysts and Performance of NSTF Based PEM Electrolyzers. Krzysztof A. Lewinski, ECS Transactions 69 (17) (2015) 893–917.

[6] H. Ito, T. Maeda, a. Nakano, Y. Hasegawa, N. Yokoi, C. Hwang, M. Ishida, a. Kato, T. Yoshida, Effect of flow regime of circulating water on a proton exchange membrane electrolyzer, International Journal of Hydrogen Energy 35 (18) (2010) 9550–9560, ISSN 03603199, doi:10.1016/j.ijhydene.2010.06.103.

[7] K. Mishima, T. Hibiki, Some characteristics of air-water two-phase flow in small diameter vertical tubes, International Journal of Multiphase Flow 22 (4) (1996) 703–712, ISSN 03019322, doi:10.1016/0301-9322(96)00010-9.

[8] H. Ito, T. Maeda, A. Nakano, C. M. Hwang, M. Ishida, A. Kato, T. Yoshida, Experimental study on porous current collectors of PEM electrolyzers, International Journal of Hydrogen Energy 37 (9) (2012) 7418–7428, ISSN 03603199.

[9] H. Ide, A. Kariyasaki, T. Fukano, Fundamental data on the gas-liquid two-phase flow in minichannels, International Journal of Thermal Sciences 46 (6) (2007) 519–530, ISSN 12900729, doi:10.1016/j.ijthermalsci.2006.07.012.

[10] T. Cubaud, C.-M. Ho, Transport of bubbles in square microchannels, Physics of Fluids 16 (12) (2004) 4575, ISSN 10706631, doi:10.1063/1.1813871.

[11] I. Dedigama, P. Angeli, K. Ayers, J. Robinson, P. Shearing, D. Tsaoulidis, D. Brett, In situ diagnostic techniques for characterisation of polymer electrolyte membrane water electrolysers - Flow visualisation and electrochemical impedance spectroscopy, International Journal of Hydrogen Energy 39 (9) (2014) 4468–4482, ISSN 03603199, doi:10.1016/j.ijhydene.2014.01.026.

[12] O. Selamet, U. Pasaogullari, D. Spernjak, D. Hussey, D. Jacobson, M. Mat, Two-phase flow in a proton exchange membrane electrolyzer visualized in situ by simultaneous neutron radiography and optical imaging, International Journal of Hydrogen Energy 38 (14) (2013) 5823–5835, ISSN 03603199, doi:10.1016/j.ijhydene.2013.02.087.

[13] F. Arbabi, A. Kalantarian, R. Abouatallah, R. Wang, J. S. Wallace, A. Bazylak, Feasibility study of using microfluidic platforms for visualizing bubble flows in electrolyzer gas diffusion layers, Journal of Power Sources 258 (2014) 142–149, ISSN 03787753, doi:10.1016/j.jpowsour.2014.02.042.

[14] M. A. Hoeh, T. Arlt, I. Manke, J. Banhart, D. L. Fritz, W. Maier, W. Lehnert, In operando synchrotron X-ray radiography studies of polymer electrolyte membrane water electrolyzers, Electrochemistry Communications 55 (2015) 55–59, ISSN 13882481, doi:10.1016/j.elecom.2015.03.009.

[15] S. S. Lafmejani, A. C. Olesen, S. K. Kær, Analysing Gas-Liquid Flow in PEM Electrolyser Micro-Channels, in: ECS Transactions, vol. 75, ISBN 9781607685395, ISSN 1938-6737, 1121–1127, doi:10.1149/07514.1121ecst, 2016.

[16] M. A. Hoeh, T. Arlt, N. Kardjilov, I. Manke, J. Banhart, D. L. Fritz, J. Ehlert, W. Lüke, W. Lehnert, In-operando Neutron Radiography Studies of Polymer Electrolyte Membrane Water Electrolyzers, ECS Transactions 69 (17) (2015) 1135–1140.

[17] J. Seweryn, J. Biesdorf, T. J. Schmidt, P. Boillat, Communication - Neutron Radiography of the Water/Gas Distribution in the Porous Layers of an Operating Electrolyser, Journal of The Electrochemical Society 163 (11) (2016) F3009–F3011, ISSN 0013-4651, doi:10.1149/2.0641607jes.

[18] C. Immerz, M. Schweins, P. Trinke, B. Bensmann, M. Paidar, T. Bystron, K. Bouzek, R. Hanke-Rauschenbach, Experimental characterization of inhomogeneity in current density and temperature distribution along a single-channel PEM water electrolysis cell, Electrochimica Acta 260 (2018) 582–588, ISSN 00134686, doi:10.1016/j.electacta.2017.12.087.

[19] B. Bensmann, R. Hanke-Rauschenbach, Engineering Modeling of PEM Water Electrolysis: A survey, E C S Transactions 75 (14) (2016) 1065–1072.

[20] J. Nie, Y. Chen, Numerical modeling of three-dimensional two-phase gas-liquid flow in the flow field plate of a PEM electrolysis cell, International Journal of Hydrogen Energy 35 (8) (2010) 3183–3197, ISSN 03603199, doi:10.1016/j.ijhydene.2010.01.050.

[21] A. C. Olesen, C. Rømer, S. K. Kær, A numerical study of the gas-liquid, two-phase flow maldistribution in the anode of a high pressure PEM water electrolysis cell, International Journal of Hydrogen Energy 41 (1) (2016) 52–68, ISSN 03603199, doi:10.1016/j.ijhydene.2015.09.140.

[22] F. Arbabi, H. Montazeri, R. Abouatallah, R. Wang, A. Bazylak, Three-Dimensional Computational Fluid Dynamics Modelling of Oxygen Bubble Transport in Polymer Electrolyte Membrane Electrolyzer Porous Transport Layers, Journal of The Electrochemical Society 163 (11) (2016) F3062–F3069, ISSN 0013-4651, doi:10.1149/2.0091611jes.

[23] S. S. Lafmejani, A. C. Olesen, S. K. Kær, VOF modelling of gas-liquid flow in PEM water electrolysis cell microchannels, International Journal of Hydrogen Energy doi:10.1016/j.ijhydene.2017.05.079.

[24] A. C. Olesen, S. K. Kær, The Effect of PFSA Membrane Compression on the Predicted Performance of a High Pressure PEM Electrolysis Cell, in: ECS Transactions, vol. 68, ISSN 1938-6737, 99–116, doi:10.1149/06803.0099ecst, 2015.

[25] K. Elsøe, L. Grahl-Madsen, G. G. Scherer, J. Hjelm, M. B. Mogensen, Electrochemical Characterization of a PEMEC Using Impedance Spectroscopy, Journal of The Electrochemical Society 164 (13) (2017) F1419–F1426, ISSN 0013-4651, doi:10.1149/2.0651713jes.

[26] S. H. Frensch, A. C. Olesen, S. S. Araya, S. K. Kær, Model-supported characterization of a PEM water electrolysis cell for the effect of compression, Electrochimica Acta 263 (2018) 228–236, doi:10.1016/j.electacta.2018.01.040.

[27] A. Serizawa, K. S. Gabriel, Multiphase Flow Handbook, in: C. T. Crowe (Ed.), CRC Press, vol. 1218, chap. 11, ISBN 0849312809, 1156, doi:10.1016/j.chroma.2011.01.063, 2006.

[28] N. Shao, A. Gavriilidis, P. Angeli, Flow regimes for adiabatic gas-liquid flow in microchannels, Chemical Engineering Science 64 (11) (2009) 2749–2761, ISSN 0009-2509, doi:10.1016/j.ces.2009.01.067.

[29] S. G. Kandlikar, W. J. Grande, Evolution of Microchannel Flow Passages-Thermohydraulic Performance and Fabrication Technology, ASME International Mechanical Engineering Congress & Exposition (2002) 1–13ISSN 00179310, doi:10.1115/IMECE2002-32043.

[30] K. Triplett, S. Ghiaasiaan, S. Abdel-Khalik, D. Sadowski, Gas-liquid two-phase flow in microchannels Part I: two-phase flow patterns, International Journal of Multiphase Flow 25 (3) (1999) 377–394, ISSN 03019322, doi:10.1016/S0301-9322(98)00054-8.

[31] F. P. Bretherton, The motion of long bubbles in tubes, Journal of Fluid Mechanics 10 (2) (1961) 166–188, doi:10.1017/S0022112061000160.

[32] M. Kawaji, P. M.-Y. Chung, Unique Characteristics of Adiabatic Gas-Liquid Flows in Microchannels: Diameter and Shape Effects on Flow Patterns, Void Fraction and Pressure Drop, in: ASME 2003 1st International Conference on Microchannels and Minichannels, ASME, 115–127, 2003.

[33] T. S. Zhao, Q. C. Bi, Co-current air-water two-phase flow patterns in vertical triangular microchannels, International Journal of Multiphase Flow 27 (5) (2001) 765–782, ISSN 03019322, doi:

10.1016/S0301-9322(00)00051-3.

[34] M. Ishii, T. Hibiki, Thermo-Fluid Dynamics of Two-Phase Flow, Springer New York, New York, NY, second edi edn., ISBN 978-1-4419-7984-1, doi:10.1007/978-1-4419-7985-8, 2011.

[35] H. A. Jakobsen, Multiphase Flow, in: Chemical Reactor Modeling SE - 3, Springer Berlin Heidelberg, ISBN 978-3-540-25197-2, 335–501, doi:10.1007/978-3-540-68622-4_3, 2008.

[36] R. B. Bird, W. E. Stewart, E. N. Lightfoot, Transport Phenomena, John Wiley & Sons, Inc., 2nd ed., edn., ISBN 0470115394, 2007.

[37] A. Z. Weber, R. L. Borup, R. M. Darling, P. K. Das, T. J. Dursch, W. Gu, D. Harvey, A. Kusoglu, S. Litster, M. M. Mench, R. Mukundan, J. P. Owejan, J. G. Pharoah, M. Secanell, I. V. Zenyuk, P. Systems, B. C. Vj, A Critical Review of Modeling Transport Phenomena in Polymer-Electrolyte Fuel Cells, Journal of The Electrochemical Society 161 (12) (2014) 1254–1299, doi:10.1149/2.0751412jes.

[38] A. Kusoglu, B. L. Kienitz, A. Z. Weber, Understanding the Effects of Compression and Constraints on Water Uptake of Fuel-Cell Membranes, Journal of The Electrochemical Society 158 (12) (2011) B1504, ISSN 00134651, doi:10.1149/2.097112jes.

[39] F. R. Menter, Two-equation eddy-viscosity turbulence models for engineering applications, AIAA Journal 32 (8) (1994) 1598–1605, ISSN 0001-1452, doi:10.2514/3.12149.

[40] H. Wu, X. Li, P. Berg, On the modeling of water transport in polymer electrolyte membrane fuel cells, Electrochimica Acta 54 (27) (2009) 6913–6927, ISSN 0013-4686.

[41] R. Guidelli, R. G. Compton, J. M. Feliu, E. Gileadi, J. Lipkowski, W. Schmickler, S. Trasatti, Defining the transfer coefficient in electrochemistry: An assessment (IUPAC Technical Report), Pure and Applied Chemistry 86 (2) (2014) 245–258, ISSN 1365-3075, doi:10.1515/pac-2014-5026.

[42] J. O. Bockris, Kinetics of Activation Controlled Consecutive Electrochemical Reactions: Anodic Evolution of Oxygen, The Journal of Chemical Physics 24 (4).

[43] J. Rossmeisl, Z. W. Qu, H. Zhu, G. J. Kroes, J. K. Nørskov, Electrolysis of water on oxide surfaces, Journal of Electroanalytical Chemistry 607 (1-2) (2007) 83–89, ISSN 00220728, doi:10.1016/j.jelechem.2006.11.008.

[44] E. Rasten, G. Hagen, R. Tunold, Electrocatalysis in water electrolysis with solid polymer electrolyte, Electrochimica Acta 48 (25-26) (2003) 3945–3952, ISSN 00134686, doi:10.1016/j.electacta.2003.04.001.

[45] E. Slavcheva, I. Radev, S. Bliznakov, G. Topalov, P. Andreev, E. Budevski, Sputtered iridium oxide films as electrocatalysts for water splitting via PEM electrolysis, Electrochimica Acta 52 (12) (2007) 3889–3894, ISSN 00134686, doi:10.1016/j.electacta.2006.11.005.

[46] M. Thomasse, S. Sunde, Electrocatalysts for Oxygen Evolution Reaction, in: D. Bessarabov, H. Wang, H. Li, N. Zhao (Eds.), PEM Electrolysis for Hydrogen Production: Principles and Applications, chap. 3, 2016.

[47] N. I. Kolev, Multiphase Flow Dynamics 2: Mechanical interactions, Springer-Verlag, Berlin Heidelberg, 4th edn., ISBN 9783642205972, doi:10.1007/978-3-642-20598-9, 2011.

[48] The Favre averaged drag model for turbulent dispersion in Eulerian multi-phase flows, 5th International Conference on Multiphase Flow (392) (2004) 1–17.

[49] A. Z. Weber, J. Newman, Transport in Polymer-Electrolyte Membranes, Journal of The Electrochemical Society 151 (2004) A311–A325.

[50] Y. Cengel, A. Ghajar, Heat and Mass Transfer: Fundamentals and Applications, McGraw-Hill Education, 5 edn., ISBN 0073398187, 2015.

[51] C. Y. Wang, Fundamental models for Fuel Cell Engineering, Chemical Review 104 (2004) 4727–4766.

[52] J. H. Nam, M. Kaviany, Effective diffusivity and water-saturation distribution in single- and two-layer PEMFC diffusion medium, International Journal of Heat and Mass Transfer 46 (24) (2003) 4595–4611, ISSN 0017-9310, doi:10.1016/S0017-9310(03)00305-3.

[53] L. M. Pant, S. K. Mitra, M. Secanell, Absolute permeability and Knudsen diffusivity measurements in PEMFC gas diffusion layers and micro porous layers, Journal of Power Sources 206 (2012) 153–160, ISSN 03787753, doi:10.1016/j.jpowsour.2012.01.099.

[54] T. Höhne, C. Vallée, F. D.-r. V, Experiments and numerical simulations of horizontal two-phase flow regimes using an interfacial area density model, Journal of Computational Multiphase Flows 2 (3) (2010) 131–143.

[55] E. C. Kumbur, K. V. Sharp, M. M. Mench, Validated Leverett Approach for Multiphase Flow in PEFC Diffusion Media, Journal of The Electrochemical Society 154 (12) (2007) B1295–B1304, doi:10.1149/1.2784283.

[56] V. Gurau, M. J. Bluemle, E. S. D. Castro, Y.-M. Tsou, T. A. Zawodzinski, Jr., J. A. Mann, Characterization of transport properties in gas diffusion layers for proton exchange membrane fuel cells: 2. Absolute permeability, Journal of Power Sources 165 (2) (2007) 793–802, ISSN 0378-7753, doi:DOI:10.1016/j.jpowsour.2006.12.068.

[57] S. Jung, Non-isothermal multi-dimensional direct methanol fuel cell model with micro-porous layers mitigating water/methanol crossover, Journal of Power Sources 231 (2013) 60–81, ISSN 03787753, doi:10.1016/j.jpowsour.2012.12.086.

[58] H. Meng, A two-phase non-isothermal mixed-domain PEM fuel cell model and its application to two-dimensional simulations, Journal of Power Sources 168 (1) (2007) 218–228, ISSN 03787753, doi:10.1016/j.jpowsour.2007.03.012.

[59] J. T. Gostick, M. W. Fowler, M. A. Ioannidis, M. D. Pritzker, Y. M. Volfkovich, A. Sakars, Capillary pressure and hydrophilic porosity in gas diffusion layers for polymer electrolyte fuel cells, Journal of Power Sources 156 (2) (2006) 375–387, ISSN 0378-7753, doi:10.1016/j.jpowsour.2005.05.086.

[60] J. Durst, C. Simon, F. Hasche, H. A. Gasteiger, Hydrogen Oxidation and Evolution Reaction Kinetics on Carbon Supported Pt, Ir, Rh, and Pd Electrocatalysts in Acidic Media, Journal of the Electrochemical Society 162 (1) (2014) F190–F203, ISSN 0013-4651, doi:10.1149/2.0981501jes.

[61] M. Espinosa-López, C. Darras, P. Poggi, R. Glises, P. Baucour, A. Rakotondrainibe, S. Besse, P. Serre-Combe, Modelling and experimental validation of a 46 kW PEM high pressure water electrolyzer, Renewable Energy 119 (2018) 160–173, ISSN 18790682, doi:10.1016/j.renene.2017.11.081.

[62] M. Chandesris, V. Médeau, N. Guillet, S. Chelghoum, D. Thoby, F. Fouda-Onana, Membrane degradation in PEM water electrolyzer: Numerical modeling and experimental evidence of the influence of temperature and current density, International Journal of Hydrogen Energy 40 (3) (2015) 1353–1366, ISSN 03603199, doi:10.1016/j.ijhydene.2014.11.111.

[63] Z. Abdin, C. J. Webb, E. M. Gray, Modelling and simulation of a proton exchange membrane (PEM) electrolyser cell, International Journal of Hydrogen Energy 40 (39) (2015) 13243–13257, ISSN 03603199, doi:10.1016/j.ijhydene.2015.07.129.

[64] P. Trinke, P. Haug, J. Brauns, B. Bensmann, T. Turek, Hydrogen Crossover in PEM and Alkaline Water Electrolysis: Mechanisms, Direct Comparison and Mitigation Strategies, Journal of The Electrochemical Society 165 (7) (2018) 502–513, doi:10.1149/2.0541807jes.

[65] S. Lafmejani, A. Olesen, S. A. Shakhshir, S. Kaer, Analysing Gas-Liquid Flow in PEM Electrolyser Micro-Channels using a Micro-Porous Ceramic as Gas Permeable wall, ECS Transactions 80 (8) (2017) 1107–1115, ISSN 1938-6737, doi:10.1149/08008.1107ecst.

[66] J. P. Owejan, T. a. Trabold, D. L. Jacobson, D. R. Baker, D. S. Hussey, M. Arif, In situ investigation of water transport in an operating PEM fuel cell using neutron radiography: Part 2 - Transient water accumulation in an interdigitated cathode flow field, International Journal of Heat and Mass Transfer 49 (25-26) (2006) 4721–4731, ISSN 00179310, doi:10.1016/j.ijheatmasstransfer.2006.07.004.

[67] T. Berning, M. Odgaard, S. K. Kær, A Computational Analysis

of Multiphase Flow Through PEMFC Cathode Porous Media Using the Multifluid Approach, Journal of the Electrochemical Society 156 (2009) B1301–B1311.

[68] P. Lettenmeier, S. Kolb, F. Burggraf, A. S. Gago, K. A. Friedrich, Towards developing a backing layer for proton exchange membrane electrolyzers, Journal of Power Sources 311 (2016) 153–158, ISSN 03787753, doi: 10.1016/j.jpowsour.2016.01.100.

[69] F. Fouda-Onana, M. Chandesris, V. Médeau, S. Chelghoum, D. Thoby, N. Guillet, Investigation on the degradation of MEAs for PEM water electrolysers part I: Effects of testing conditions on MEA performances and membrane properties, International Journal of Hydrogen Energy 41 (38) (2016) 16627–16636, ISSN 03603199, doi:10.1016/j.ijhydene.2016.07.125.

[70] F. Bauer, S. Denneler, M. Willert-Porada, Influence of temperature and humidity on the mechanical properties of Nafion?? 117 polymer electrolyte membrane, Journal of Polymer Science, Part B: Polymer Physics 43 (7) (2005) 786–795, ISSN 08876266, doi:10.1002/polb.20367.

[71] F. Nandjou, J.-P. Poirot-Crouveziera, M. Chandesrisa, J.-F. Blachota, C. Bonnaud, Y. Bultelc, Correlation Between Local Temperature and Degradations in Polymer Electrolyte Membrane Fuel Cells F. Nandjou 66 (25) (2015) 1–12.